S. Massaglia
G. Bodo
A. Mignone
P. Rossi (Eds.)

Jets From Young Stars III

Numerical MHD and Instabilities

Springer

Editors

Silvano Massaglia
Università di Torino
Dipto. Fisica Generale
Via Pietro Giuria, 1
10125 Torino
Italy
massaglia@ph.unito.it

Gianluigi Bodo
Osservatorio Astronomico di
Torino
Strada Osservatorio, 20
10025 Pino Torinese TO
Italy
bodo@to.astro.it

Andrea Mignone
Università di Torino
Dipto. Fisica Generale
Via Pietro Giuria, 1
10125 Torino
Italy
mignone@ph.unito.it

Paola Rossi
INAF Osservatorio
di Torino Astronomico
Viale Osservatorio, 20
10025 Pino Torinese
Italy
rossi@to.astro.it

Massaglia, S. et al. (Eds.), *Jets From Young Stars III*, Lect. Notes Phys. 754 (Springer, Berlin Heidelberg 2008), DOI 10.1007/ 978-3-540-76967-5

ISBN: 978-3-540-76966-8 e-ISBN: 978-3-540-76967-5

DOI 10.1007/978-3-540-76967-5

Lecture Notes in Physics ISSN: 0075-8450 e-ISSN: 1616-6361

Library of Congress Control Number: 2008927516

Cover design: eStudio Calamar S.L., F. Steinen-Broo, Pau/Girona, Spain

Printed on acid-free paper

9 8 7 6 5 4 3 2 1

springer.com

Preface

The study of the mechanisms that govern origin and propagation of stellar jets involves the treatment of many concurrent physical processes such as gravitation, hydrodynamics and magnetohydrodynamics, atomic physics and radiation. In the past years, an intensive work has been done looking for solutions of the ideal MHD equations in the steady state limit as well as studying the stability of outflows in the linear regime. These kind, of approaches have provided a contribution to the understanding of jets that can hardly be overestimated. However, the extension of the analyses to the time-dependent and nonlinear regimes could not be avoided, and the MHD numerical simulations were the only mean to achieve this goal.

In the recent years, considerable progresses have been made by the computational fluid dynamic community in the development of numerical techniques, the so-called high resolution shock capturing schemes, well suited for the treatment of supersonic flows with discontinuities. The numerical simulations of astrophysical jets took advantage of these developments; however new physics needed to be incorporated, such as magnetic field effects, radiation losses by diluted gases, and proper astrophysics environments. These needs led to the nontrivial extension of the methods devised for the Euler equations of gasdynamics to the magneto-hydrodynamical system. On the other hand, the possibility of carrying out numerical calculations has been greatly facilitated by the availability, on one hand, of powerful supercomputers and, on the other hand, of fast processors at low cost. Large scale 3D simulations of jets at high resolution are now possible thanks to supercomputers, but also high resolution 2D MHD simulations can be performed routinely on desktop computers. These possibilities have greatly extended our understanding of jets, and numerical simulations are now an essential tool for investigating the physics of such objects.

This book collects the lectures from the third JETSET school, Jets from Young Stars III: Numerical MHD and Instabilities, held in Sauze d'Oulx in January 2007. The aim of this school was to introduce PhD students and young researchers to the basic methods in computational hydrodynamics and

magneto-hydrodynamics as well as to review some of the most relevant instabilities in astrophysical outflows.

The book is divided in two parts. In the first one, Eleuterio Toro presents and discusses the basic numerical methods in hydrodynamics, their stability, monotonicity and accuracy properties, and introduces different Riemann solvers and flux limiter methods. Andrea Mignone and Gianluigi Bodo then extend the discussion to MHD, examining, in particular, the various methods devised to overcome the numerical difficulties intrinsic to the MHD equations. The second part is devoted to hydrodynamic and MHD instabilities, such as the Kelvin–Helmholtz instabilities, treated by Edoardo Trussoni, the pressure driven instabilities, by Pierre-Yves Longaretti, the thermal instabilities, by Gianluigi Bodo, and the instabilities in radiative shocks, by Andrea Mignone.

The editors are grateful to the lecturers for their presentations and efforts to contribute to this book, and to Ovidiu Tesileanu and Titos Matsakos that have been of great help in the organization of the school. Thanks also to Eileen Flood and Gabriella Ardizzoia for their precious help in managing the life of the participants during the days of the school. The editors acknowledge the invaluable contribution and support by Emma Whelan for taking care of the book editing.

Torino — *Silvano Massaglia*
Andrea Mignone
Pino Torinese — *Gianluigi Bodo*
Paola Rossi

Contents

Shock-Capturing Schemes in Computational MHD

A. Mignone[1,2] and G. Bodo[1]

[1] INAF Osservatorio Astronomico di Torino, 10025 Pino Torinese, Italy, mignone@to.astro.it
[2] Dipartimento di Fisica Generale dell'Università, Via Pietro Giuria 1, I-10125 Torino, Italy, bodo@to.astro.it

Abstract. The purpose of the present review is to present and discuss some introductory aspects relevant to computational compressible magnetohydrodynamics (MHD). The shock-capturing framework developed for the Euler equations of gasdynamics is extended to MHD by illustrating differences and additional complexities introduced by the presence of magnetic fields. In particular, we focus our attention on the characteristic structure of the equations by investigating the nature of different MHD waves, the solution to the Riemann problem and last, but not least, various computational strategies to control the divergence-free condition of magnetic fields.

Keywords Magnetohydrodynamics (MHD) · Methods: numerical · Shock waves · Waves

1 Introduction

Astrophysical plasmas can often be described by means of the ideal compressible magnetohydrodynamic (MHD) equations. A far from exhaustive list includes jets, accretion disks, stellar or galactic atmospheres, and the interstellar medium. In many instances, one has to deal with flows with shocks and discontinuities, and, in such situations, the numerical methods used in the simulations are based on the shock-capturing framework developed for the Euler equations of gasdynamics. The extension of such framework to MHD has proven, however, to be nontrivial because of several properties of the MHD system that makes it different from the Euler counterpart. A first example of the problems encountered when moving from gasdynamic to MHD is nonstrict hyperbolicity. This has been addressed by [5] and [40], and following this and other advancements, several second-order upwind codes were then constructed and tested mainly for the one-dimensional case, see for example [2, 42, 50] and [10]. New problems have to be considered for the

Mignone, A., Bodo, G.: *Shock-Capturing Schemes in Computational MHD*. Lect. Notes Phys. **754**, 71–101 (2008)
DOI 10.1007/978-3-540-76967-5_2

multidimensional case, in particular MHD equations are supplemented by the condition of null divergence of the magnetic field that has to be preserved during the evolution. A failure of the numerical scheme to maintain this constraint, as shown by [4], leads to unphysical effects in the solution. Several different methods have then been proposed for dealing with this issue, see for example [3, 4, 12, 17, 19, 29, 36].

In this review, after a presentation of the equations in Sect. 2, we will discuss their characteristic structure and the nature of the waves with particular reference to the peculiarities of the MHD system in Sect. 3. The solution to the Riemann problem is one of the main building blocks of shock capturing methods, and our discussion will be focused on approximate solvers, in particular, of the HLL class. In the last section, we will deal with the other big issue of computational MHD and will present several different computational strategies for approaching the divergence free constraint.

2 The MHD Equations

The macroscopic dynamics of a plasma can be described, in many instances, by the MHD equations. Describing the plasma, as a single fluid, in terms of density ρ, velocity $\boldsymbol{v}$, thermal pressure p_g, and magnetic field $\mathbf{B}$, the MHD equations take the form

$$\frac{\partial \rho}{\partial t} = -\nabla \cdot (\rho \mathbf{v}) \,, \tag{1}$$

$$\rho \frac{\partial \mathbf{v}}{\partial t} = -\rho \mathbf{v} \cdot \nabla \mathbf{v} - \nabla p_g + \mathbf{J} \times \mathbf{B}, \tag{2}$$

$$\frac{\partial p_g}{\partial t} = -\nabla \cdot (p_g \boldsymbol{v}) - (\Gamma - 1) \left(p_g \nabla \cdot \boldsymbol{v} - \eta \mathbf{J}^2 \right) \,, \tag{3}$$

$$\frac{\partial \mathbf{B}}{\partial t} = -\nabla \times \mathbf{\Omega}, \tag{4}$$

$$\mathbf{J} = \nabla \times \mathbf{B} \,, \tag{5}$$

$$\mathbf{\Omega} = -\mathbf{v} \times \mathbf{B} + \eta \mathbf{J} \,, \tag{6}$$

where $\mathbf{\Omega}$ denotes the electric field. The units of $\mathbf{B}$ are chosen such that the magnetic permeability of vacuum becomes equal to unity, $\mu_0 = 1$. In Eq. (5), expressing the current density $\mathbf{J}$ in terms of the magnetic field, we neglected the displacement current $\partial \mathbf{\Omega} / \partial t$. This is justified if we are far from the relativistic regime, i.e., $v \ll c$. Eq. (6) is the Ohm's law and η is the resistivity. With respect to the Euler system of gasdynamics, we have, in Eq. (2), the additional term $\mathbf{J} \times \mathbf{B}$ that represents the Lorentz force and in Eq. (3) the Joule heating term $\eta \mathbf{J}^2$. Moreover, we have the additional induction equation (4) for the evolution of the magnetic field. The condition $\nabla \cdot \mathbf{B} = 0$

represents a constraint that has to be satisfied by the magnetic field at all times, and Eq. (4) ensures that if it is fulfilled at $t = 0$ it will be so at any time. In system (1, 2, 3, 4, 5, 6) and in the rest of the Section, we keep the resistive terms for completeness although we will not discuss their numerical treatment.

Shock capturing methods are based on the conservation form that, for the above system, can be written as:

$$\frac{\partial \rho}{\partial t} = -\nabla \cdot (\rho \mathbf{v}) \,, \tag{7}$$

$$\frac{\partial \rho \mathbf{v}}{\partial t} = -\nabla \cdot \left(\rho \boldsymbol{v}\boldsymbol{v} + \mathbf{I} p_g + \mathbf{I}\frac{\mathbf{B}^2}{2} - \mathbf{B}\mathbf{B} \right) , \tag{8}$$

$$\frac{\partial E}{\partial t} = -\nabla \cdot \left(\mathbf{v}\,(E + p_g) + \mathbf{v} \cdot \left(\mathbf{I}\frac{\mathbf{B}^2}{2} - \mathbf{B}\mathbf{B} \right) - \mathbf{B} \times \eta \mathbf{J} \right) , \tag{9}$$

$$\frac{\partial \mathbf{B}}{\partial t} = \nabla \times (\mathbf{v} \times \mathbf{B} - \eta \mathbf{J}) \,, \tag{10}$$

where $\mathbf{I}$ is the unit dyadic and the total energy density E is defined as

$$E = \frac{p_g}{\Gamma - 1} + \frac{\rho \boldsymbol{v}^2}{2} + \frac{\mathbf{B}^2}{2} \,. \tag{11}$$

The above conservation equations can be written in the compact form

$$\frac{\partial \mathbf{U}}{\partial t} + \nabla \cdot \mathbf{F} = \mathbf{0} \,, \tag{12}$$

where the vector $\mathbf{U}$ of conserved quantities and the vector $\mathbf{F}$ of fluxes, neglecting resistivity, are given, respectively, by

$$\mathbf{U} = \begin{pmatrix} \rho \\ \rho \boldsymbol{v} \\ E \\ \mathbf{B} \end{pmatrix} , \quad \mathbf{F} = \begin{bmatrix} \rho \boldsymbol{v} \\ \rho \boldsymbol{v}\boldsymbol{v} + \mathbf{I} p - \mathbf{B}\mathbf{B} \\ (E + p)\, \boldsymbol{v} - (\boldsymbol{v} \cdot \mathbf{B})\, \mathbf{B} \\ \boldsymbol{v}\mathbf{B} - \mathbf{B}\boldsymbol{v} \end{bmatrix} , \tag{13}$$

where $p = p_g + \mathbf{B}^2/2$ denotes the total pressure.

3 The Riemann Problem in MHD

The solution to the Riemann problem in magnetohydrodynamics is paved by several additional complications when compared to the underlying hyperbolic system of the Euler equation of gasdynamics. The increased complexity cannot

be ascribed just to the increased number of waves due to a larger number of equations, but also to the fact that the system is non strictly hyperbolic with non convex flux function, and the characteristic fields are no longer either genuinely non linear or linearly degenerated. In this respect, non regular waves like compound waves and overcompressive intermediate shocks may be formed in MHD.

As usual, one starts with the problem definition, i.e., a discontinuity separating a pair of arbitrary constant left and right states,

$$\boldsymbol{U}(x, t=0) = \begin{cases} \boldsymbol{U}_{\rm L} & \text{for} \quad x < 0, \\ \boldsymbol{U}_{\rm R} & \text{for} \quad x > 0\,. \end{cases} \tag{14}$$

As with hydrodynamics Riemann solvers, the initial jump will decay into a set of uniform states separated by left- and right-facing shock and rarefaction waves. In general, at $t > 0$, the full structure comprises a total of eight states (including the original ones) separated by seven waves, see Fig. 1. With the exception of the entropy mode associated with a contact discontinuity moving at the speed of the fluid, the other six waves are related to fast, Alfvén, and slow characteristics and can be either shocks or rarefactions. In addition to this, two families of waves may occasionally have the same speeds or develop compound wave structures where both a shock and a rarefaction propagate

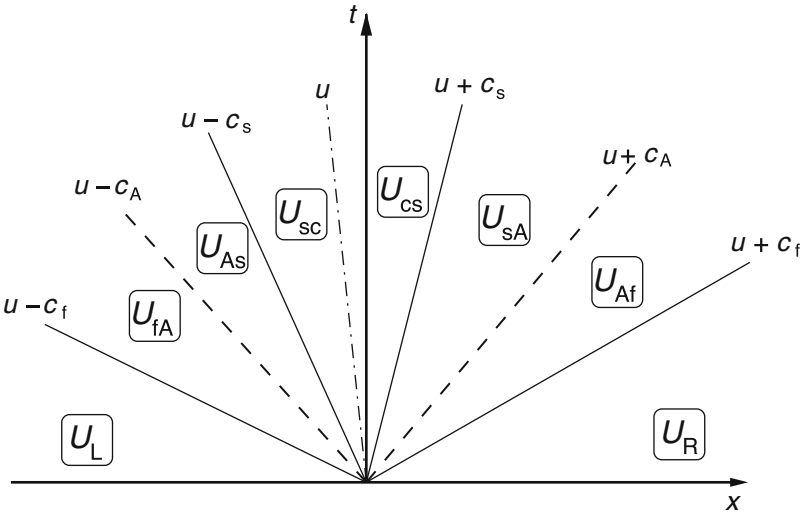

Fig. 1. General structure of the Riemann fan generated by two initial constant state $\boldsymbol{U}_{\rm L}$ and $\boldsymbol{U}_{\rm R}$. The pattern comprises seven waves corresponding to a pair of fast ($u \pm c_{\rm f}$), Alfvén ($u \pm c_{\rm A}$), slow ($u \pm c_{\rm s}$) modes separated by a contact discontinuity in the middle (u). The waves bound six new constant states, from left to right, $\boldsymbol{U}_{\rm fA}$, $\boldsymbol{U}_{\rm As}$, $\boldsymbol{U}_{\rm sc}$, $\boldsymbol{U}_{\rm cs}$, $\boldsymbol{U}_{\rm sA}$, $\boldsymbol{U}_{\rm Af}$

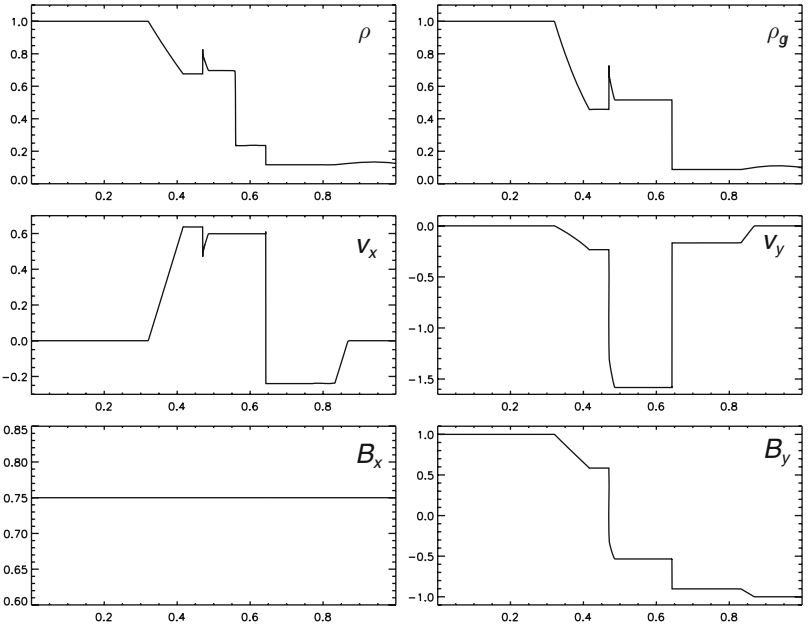

Fig. 2. The Brio-Wu shock tube problem. From left to right, the solution involves five waves: a *fast rarefaction wave*, a *slow compound wave*, a *contact wave*, a slow shock, and a fast rarefaction. Here $\Gamma = 2$. Density and pressure are shown in the *top* panels, velocities in the *middle* ones, and magnetic fields in the *bottom* panels. Results have been obtained using an adaptive grid with an equivalent resolution of $12,800$ grid zones

adjacent to one another. An example of such situation is encountered in the Brio and Wu [5] shock tube problem, with initial left and right data given by $(\rho, p_g)_{\rm L} = (1, 1)$, $\mathbf{B}_{\rm L} = (3/4, 1, 0)$, $\boldsymbol{v}_{\rm L} = \boldsymbol{v}_{\rm R} = \mathbf{0}$, $(\rho, p_g)_{\rm R} = (1/8, 1/10)$ and $\boldsymbol{B}_{\rm R} = (3/4, -1, 0)$. The results computed with the PLUTO code [34] are shown in Fig. 2: a compound structure consisting of a slow compressive shock and a rarefaction is clearly visible at $x \approx 0.46$. This peculiar behavior is a direct consequence of the fact that the MHD system of equations are neither strictly hyperbolic nor strictly convex. For these reasons, unlike the Euler equations of gasdynamics, a closed form solution to the Riemann problem in MHD cannot be found.

Instead, accurate solvers may be constructed in the regular case by proceeding as for the hydrodynamical problem, [7, 8, 9, 18, 42, 50]. This demands the simultaneous solution of the Rankine-Hugoniot jump conditions across each wave by a self-consistent procedure that resolves fast, slow, and Alfvén waves to the left and right of the contact (tangential in the degenerate case) discontinuity, always located at the center of the structure.

3.1 Discontinuities

The jump conditions can be derived directly from the original conservation law by integrating across a discontinuous surface. They are better expressed in Lagrangian mass coordinates,

$$\begin{aligned} W\left[\frac{1}{\rho}\right] &= -\left[u\right], \\ W\left[u\right] &= \left[p\right], \\ W\left[\boldsymbol{v}_t\right] &= -B_x\left[\boldsymbol{B}_t\right], \\ W\left[\frac{\boldsymbol{B}_t}{\rho}\right] &= -B_x\left[\boldsymbol{v}_t\right], \\ W\left[\frac{E}{\rho}\right] &= \left[up\right] - B_x\left[\boldsymbol{B}\cdot\boldsymbol{v}\right], \end{aligned} \tag{15}$$

where W is the mass flux entering a discontinuity surface and $[\cdot]$ is the difference between the two states on each side of the front.

In the previous equations, $p = p_g + \boldsymbol{B}^2/2$ denotes the total pressure, u and B_x are the projections of the velocity and magnetic field vectors on the discontinuity normal, and the subscript t refers to the tangential components. Note also that the normal component of magnetic field, B_x, is constant throughout the Riemann fan and should be regarded as a parameter.

Rotational waves are linear waves characterized by

$$\left[u\right] = \left[p_g\right] = \left[\boldsymbol{B}_t^2\right] = \left[\rho\right] = 0\,. \tag{16}$$

Thus thermodynamical quantities such as density and pressure remain unaltered across the discontinuity and only tangential components can change. Indeed, vector fields experience a rotation without changing their magnitude, meaning that the total pressure is also continuous, i.e., $[p] = 0$. For this reason, a rotational discontinuity cannot be formed by the steepening of a smooth disturbance. Rotational waves propagate at the Alfvén speed relative to the fluid, $u \pm B_x/\sqrt{\rho}$.

Shock waves are physically admissible if the entropy is increased through the front. Through a shock wave, all hydrodynamics variables including density, pressure, velocity, and magnetic fields are subjected to a jump. From the third and fourth equations in (15), one sees that the magnetic field on both sides of the shock lies on the same plane and no rotation takes place. Thus only the magnitude of the field can change.

A fast shock is characterized by an increased magnitude of the transverse magnetic field when passing from the pre shock to the post shock state [7, 25]. This has the consequence to bend the field lines away from the shock normal. The downstream magnetic field, however, is not a monotonic function of the Mach number for sufficiently large values of B_x. This

means that the transverse component of $\boldsymbol{B}$ in the downstream state does not determine the post shock values uniquely [18, 25].

Through a slow shock, on the contrary, the magnitude of the transverse component of magnetic field decreases from the upstream to the downstream state. In this case, the magnetic field bends towards the shock normal. Slow shocks are more peculiar than fast shocks [47], since all the familiar quantities (i.e., pressure, density, and transverse field) do not behave in a monotonic way. Furthermore, the range of Mach number values for which a slow shock can exist is finite.

Shocks propagating in the direction of the magnetic field are called parallel shocks. In this case, $\boldsymbol{B}_t$ vanishes on both sides of the discontinuity (although $B_x \neq 0$) and the shock becomes purely hydrodynamical. In the case of a fast shock, however, another solution exists where the tangential magnetic field vanishes ahead of the front but $\boldsymbol{B}_t \neq 0$ in the downstream region. Such a particular configuration is called a *switch-on* shock, since the magnetic field is "turned-on" behind the shock. In the frame of the front, the downstream fluid moves at the local Alfvén velocity. It is worth mentioning that switch-on shocks only exist in a small range of upstream parameters [26], namely $B_x^2 > \Gamma p$ and

$$1 < M_A < \sqrt{\frac{\Gamma(1-\beta)+1}{\Gamma-1}}\,, \tag{17}$$

where $M_A = v/c_\mathrm{A}$ is the Alfvénic Mach number and $\beta = 2p/B_x^2$ is the plasma β. A reverse situation is encountered in the case of a slow shock; in this case $\boldsymbol{B}_t$ is zero in the downstream region, while it does not vanish in the upstream. This configuration corresponds to a *switch-off* shock, since the post shock magnetic field is switched off. Such fronts propagate at the Alfvén speed of the upstream medium.

When $B_x = 0$, we have a perpendicular (normal) shock. From the jump conditions (15), one immediately sees that the tangential velocity does not change through the discontinuity and the magnetic field is compressed by the same ratio as for the density, without changing its direction.

Figure 3 shows the wave pattern emerging from an initial jump [2] separating a left state with $(\rho, p)_\mathrm{L} = (1.08, 0.95)$, $\boldsymbol{v}_\mathrm{L} = (1.2, 0.01, 0.5)$, $\boldsymbol{B}_\mathrm{L} = (2, 3.6, 2)/\sqrt{4\pi}$ from a right state with $(\rho, p)_\mathrm{R} = (1, 1)$, $\boldsymbol{v}_\mathrm{R} = \boldsymbol{0}$, $\boldsymbol{B}_\mathrm{R} = (2, 4, 2)/\sqrt{4\pi}$. As it can be seen, the solution involves discontinuities only; two opposite moving fast shocks followed by two rotational waves and slow shocks. The contact discontinuity is located at the center of the structure. Computations have been carried with $\Gamma = 5/3$ using the PLUTO code together with the Roe Riemann solver described below.

3.2 Rarefaction Waves

Fast and slow modes allow gas expansion by rarefaction waves. Across them, flow variables experience a smooth transition and the admissible states may be

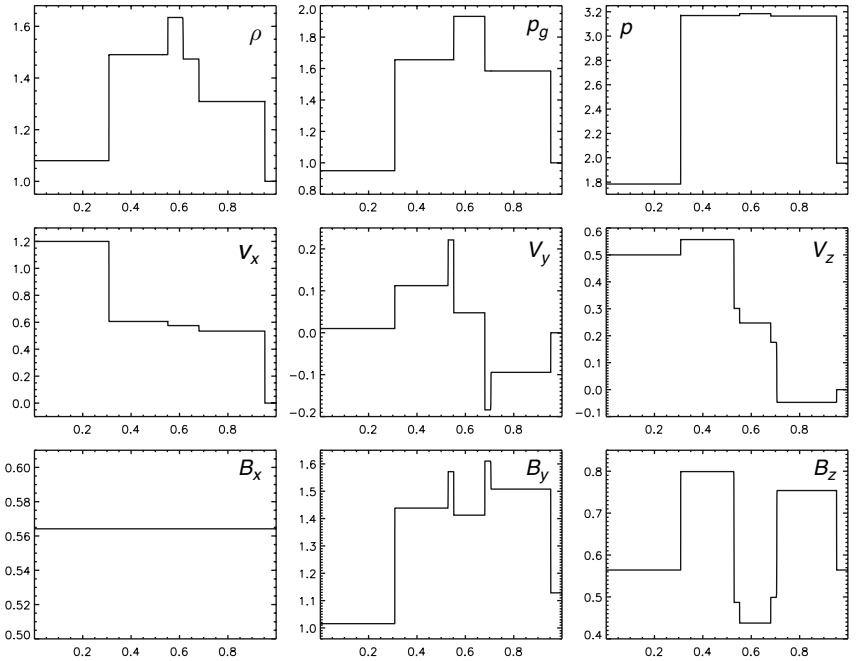

Fig. 3. A shock tube problem. Density, thermal, and total pressures are plotted in the *top* panels. Velocity and magnetic field components are shown in the *middle* and *bottom* panels, respectively. The outcoming wave structure involves two outermost fast shocks, enclosing two *rotational waves* containing two slow shocks separated by a *contact wave*

found from the integral curves which follow the eigenvectors of the hyperbolic system. Given the decomposition of the Jacobian matrix $\partial \boldsymbol{F}(\boldsymbol{U})/\partial \boldsymbol{U}$ in terms of right and left ortho-normal eigenvectors $\boldsymbol{R}_k, \boldsymbol{L}_k$ ($\boldsymbol{R}_k \cdot \boldsymbol{L}_m = \delta_{km}$) associated with eigenvalues λ_k, one can proceed as for the hydrodynamical case, that is, by replacing the set of jump conditions (15) with a set of ordinary differential equations:

$$\frac{d\boldsymbol{U}}{d\sigma} = \boldsymbol{R}_k \,, \tag{18}$$

where σ is a parameter along the curve. Equation (18) implies conservation of all Riemann invariants

$$dw_m \equiv \boldsymbol{L}_m \cdot d\boldsymbol{U} = 0 \qquad \text{for} \qquad m \neq k \,, \tag{19}$$

not associated with the wave involved. It can be shown [47] that, in contrast to a shock wave, the transverse components of the magnetic field always decrease through a fast rarefaction and increase through a slow one. As for the hydrodynamical case, the entropy is constant throughout the Riemann fan.

3.3 Approximate Riemann Solvers

In what follows, we will restrict our attention to the one-dimensional set of MHD equations written in conservation form,

$$\frac{\partial \boldsymbol{U}}{\partial t} + \frac{\partial \boldsymbol{F}}{\partial x} = 0\,, \tag{20}$$

with conservative variables and fluxes given, respectively, by

$$\boldsymbol{U} = \begin{pmatrix} \rho \\ \rho u \\ \rho \boldsymbol{v}_t \\ B_x \\ \boldsymbol{B}_t \\ E \end{pmatrix}, \quad \boldsymbol{F} = \begin{pmatrix} \rho u \\ \rho u^2 + p - B_x^2 \\ \rho \boldsymbol{v}_t u - \boldsymbol{B}_t B_x \\ 0 \\ \boldsymbol{B}_t u - \boldsymbol{v}_t B_x \\ (E+p)u - (\boldsymbol{v}\cdot\boldsymbol{B})B_x \end{pmatrix}. \tag{21}$$

The discrete version of Eq. (20) takes the difference form

$$\boldsymbol{U}_i^{n+1} = \boldsymbol{U}_i^n - \frac{\Delta t}{\Delta x}\left(\hat{\boldsymbol{f}}_{i+\frac{1}{2}} - \hat{\boldsymbol{f}}_{i-\frac{1}{2}}\right). \tag{22}$$

The numerical flux functions $\hat{\boldsymbol{f}}$ are computed at each cell interface $i+\frac{1}{2}$ by solving a Riemann problem between suitable left and right input states. For a first-order scheme, these states are provided by $\boldsymbol{U}_i^n$ and $\boldsymbol{U}_{i+1}^n$, respectively.

Nonlinear methods are based on the simultaneous solution of the Rankine Hugoniot jump conditions (15) or the smooth relations (18) across all waves in the system. The strategy proceeds by linking each constant state inside the Riemann fan with the next adjacent one, by exploiting the properties of the wave separating them. Approximate nonlinear solutions have been presented by [7, 8, 9], which treat rarefaction waves as discontinuities ("rarefaction shocks"). This simplification is sufficiently accurate in the limit of weak rarefactions and/or small time steps, such as the ones typically used in explicit methods. Exact Riemann solvers that correctly treat rarefaction waves have been proposed by [18, 42].

In either case (exact or approximate), nonlinear methods are rather involved and computationally intensive. This has motivated the probe of simplified, more efficient strategies of solution based on different levels of approximation. Indeed, the most popular methods nowadays adopted for the solution of the Riemann problem in computational MHD lean on approximate solvers. In what follows, we present a brief overview of the most popular approaches adopted.

Lax-Friedrichs and Rusanov Solvers

Perhaps the simplest approximation comes from the Lax-Friedrichs or Rusanov fluxes. The original Lax-Friedrichs method results from the attempt of stabilizing the unstable FTCS (forward in time, central in space) discretization. Specifically, one has

$$\hat{\boldsymbol{f}} = \frac{1}{2}\left[\boldsymbol{F}_{\rm L} + \boldsymbol{F}_{\rm R} - c\,(\boldsymbol{U}_{\rm R} - \boldsymbol{U}_{\rm L})\right], \tag{23}$$

where $\boldsymbol{F}_{\rm L} \equiv \boldsymbol{F}(\boldsymbol{U}_{\rm L})$ and $\boldsymbol{F}_{\rm R} \equiv \boldsymbol{F}(\boldsymbol{U}_{\rm R})$. Choosing $c = \Delta x/\Delta t$ yields the original Lax-Friedrichs scheme [27]. A considerably less diffusive variant is given by the Rusanov flux [41], where c is taken to be the maximum signal velocity $|\lambda_{\rm max}|$. For the MHD equations, the obvious choice is

$$\lambda_{\rm max} = |u| + c_{\rm f}, \tag{24}$$

where both u and $c_{\rm f}$ may be evaluated using the average state $\boldsymbol{U}_{\rm RL} = (\boldsymbol{U}_{\rm L} + \boldsymbol{U}_{\rm R})/2$.

The Rusanov flux is computationally inexpensive and straightforward to implement, since it does not require any characteristic information. Numerical experience shows that the scheme is quite robust and well-behaved, although rather diffusive, since all the knowledge about the wave structure inside the Riemann problem is avoided.

The Scheme of Harten–Lax–van Leer (HLL)

The HLL method, originally devised by Harten, Lax, and van Leer [22] for classical gasdynamics, has gained increasing popularity among researchers in the last decades.

The HLL scheme is formulated in terms of an integral average across the Riemann fan provided the leftmost ($\lambda_{\rm L}$) and rightmost ($\lambda_{\rm R}$) signal speeds can be estimated. This leads to an approximation of the Riemann fan structure where all the intermediate wave patterns are averaged into a single constant state bounded by two outermost waves, see Fig. 4. In other words, the solution to the Riemann problem on the $x/t = 0$ axis consists of three possible constant states:

$$\boldsymbol{U}(0,t) = \begin{cases} \boldsymbol{U}_{\rm L} & \text{if} \quad \lambda_{\rm L} \geq 0, \\ \boldsymbol{U}^{\rm hll} & \text{if} \quad \lambda_{\rm L} \leq 0 \leq \lambda_{\rm R}, \\ \boldsymbol{U}_{\rm R} & \text{if} \quad \lambda_{\rm R} \leq 0\,. \end{cases} \tag{25}$$

The single state $\boldsymbol{U}^{\rm hll}$ is constructed from an a priori estimate of the fastest and slowest signal velocities $\lambda_{\rm L}$ and $\lambda_{\rm R}$:

$$\boldsymbol{U}^{\rm hll} = \frac{\lambda_{\rm R}\boldsymbol{U}_{\rm R} - \lambda_{\rm L}\boldsymbol{U}_{\rm L} + \boldsymbol{F}_{\rm L} - \boldsymbol{F}_{\rm R}}{\lambda_{\rm R} - \lambda_{\rm L}}\,, \tag{26}$$

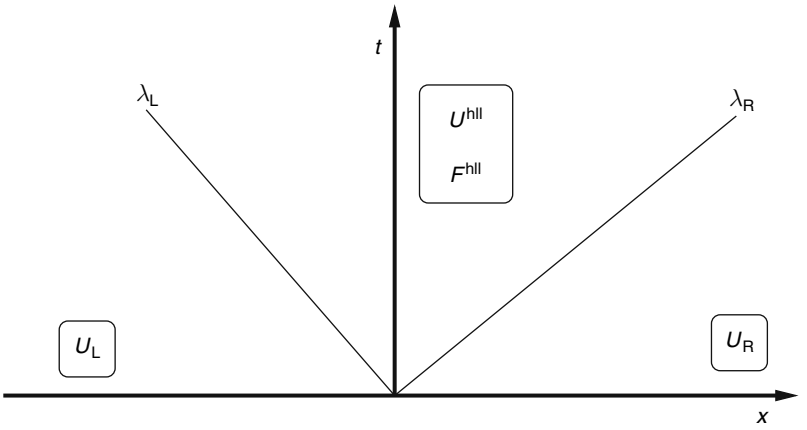

Fig. 4. Approximate structure of the Riemann fan used in the HLL solver: the whole fan has been lumped into a single state $\boldsymbol{U}^{\rm hll}$ and flux $\boldsymbol{F}^{\rm hll}$

where $\boldsymbol{F}_{\rm L} = \boldsymbol{F}(\boldsymbol{U}_{\rm L})$, $\boldsymbol{F}_{\rm R} = \boldsymbol{F}(\boldsymbol{U}_{\rm R})$. Notice that Eq. (26) represents the integral average of the solution of the Riemann problem over the wave fan [46]. Demanding consistency with the jump condition across either of the bounding waves, the corresponding interface numerical flux can be derived as:

$$\hat{\boldsymbol{f}} = \begin{cases} \boldsymbol{F}_{\rm L} & \text{if} \quad \lambda_{\rm L} \geq 0, \\ \boldsymbol{F}^{\rm hll} & \text{if} \quad \lambda_{\rm L} \leq 0 \leq \lambda_{\rm R}, \\ \boldsymbol{F}_{\rm R} & \text{if} \quad \lambda_{\rm R} \leq 0\,, \end{cases} \tag{27}$$

where

$$\boldsymbol{F}^{\rm hll} = \frac{\lambda_{\rm R}\boldsymbol{F}_{\rm L} - \lambda_{\rm L}\boldsymbol{F}_{\rm R} + \lambda_{\rm R}\lambda_{\rm L}(\boldsymbol{U}_{\rm R} - \boldsymbol{U}_{\rm L})}{\lambda_{\rm R} - \lambda_{\rm L}}\,. \tag{28}$$

Thus, given an estimate for the fastest and slowest signal speeds $\lambda_{\rm R}$ and $\lambda_{\rm L}$, an approximate solution to the Riemann problem can be constructed and the intercell numerical flux is computed according to (27). Note that, in the supersonic case ($\lambda_{\rm L} > 0$ or $\lambda_{\rm R} < 0$), the HLL approximation gives the exact solution by selecting the correct upwind flux.

The algorithm is complete once $\lambda_{\rm L}$ and $\lambda_{\rm R}$ have been specified. Several estimates have been proposed, see for example [15, 16, 45, 46]. A popular choice [15], for example, is to compute the signal velocities using the data available in the left and right states, and then define

$$\lambda_{\rm L} = \min\left[\lambda_-(\boldsymbol{U}_{\rm L}), \lambda_-(\boldsymbol{U}_{\rm R})\right], \quad \lambda_{\rm R} = \max\left[\lambda_+(\boldsymbol{U}_{\rm L}), \lambda_+(\boldsymbol{U}_{\rm R})\right]. \tag{29}$$

The HLL approach does not require a full characteristic decomposition of the equations and, for this reason, it is straightforward to implement in any functioning MHD code. Besides its computational efficiency and ease of

implementation, the HLL scheme has the attractive feature of being positively conservative in the sense that preserve initially positive densities, energies, and pressures. Despite its reliability, however, it lacks the ability to resolve intermediate structures such as Alfvén, slow, and contact modes. This results in a more diffusive behavior than other more sophisticated algorithms.

The HLLC Approximate Riemann Solver

The HLLC scheme [1, 45] improves over HLL by replacing the single averaged state defined by (26) with two approximate states, $\boldsymbol{U}^*_{\rm L}$ and $\boldsymbol{U}^*_{\rm R}$. These two states are separated by a middle wave which is assumed to have constant speed λ^*,

$$\boldsymbol{U}(0,t) = \begin{cases} \boldsymbol{U}_{\rm L} & \text{if} \quad \lambda_{\rm L} \geq 0, \\ \boldsymbol{U}^*_{\rm L} & \text{if} \quad \lambda_{\rm L} \leq 0 \leq \lambda^*, \\ \boldsymbol{U}^*_{\rm R} & \text{if} \quad \lambda^* \leq 0 \leq \lambda_{\rm R}, \\ \boldsymbol{U}_{\rm R} & \text{if} \quad \lambda_{\rm R} \leq 0, \end{cases} \tag{30}$$

and the corresponding inter cell numerical fluxes become

$$\hat{\boldsymbol{f}} = \begin{cases} \boldsymbol{F}_{\rm L} & \text{if} \quad \lambda_{\rm L} \geq 0, \\ \boldsymbol{F}^*_{\rm L} & \text{if} \quad \lambda_{\rm L} \leq 0 \leq \lambda^*, \\ \boldsymbol{F}^*_{\rm R} & \text{if} \quad \lambda^* \leq 0 \leq \lambda_{\rm R}, \\ \boldsymbol{F}_{\rm R} & \text{if} \quad \lambda_{\rm R} \leq 0. \end{cases} \tag{31}$$

This configuration is schematically depicted in Fig. 5.

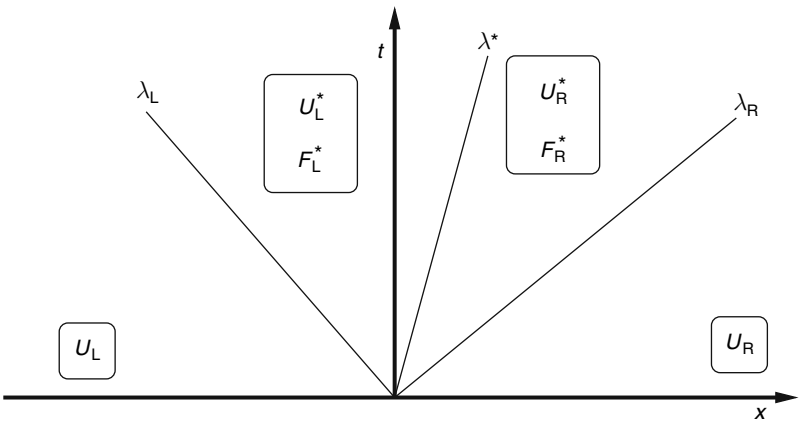

Fig. 5. Approximate structure to the Riemann fan used by the HLLC solver: the whole fan has been reduced to two single states, $\boldsymbol{U}^*_{\rm L}$ and $\boldsymbol{U}^*_{\rm R}$, separated by a *middle wave* λ^*

Note that, even if $\boldsymbol{F}_\alpha \equiv \boldsymbol{F}(\boldsymbol{U}_\alpha)$ for $\alpha = \{L, R\}$, one cannot take $\boldsymbol{F}^*_\alpha = \boldsymbol{F}(\boldsymbol{U}^*_\alpha)$. The intermediate fluxes $\boldsymbol{F}^*_{\rm L}$ and $\boldsymbol{F}^*_{\rm R}$, in fact, should be computed consistently from the Rankine-Hugoniot jump conditions across each wave:

$$\lambda_\alpha \left(\boldsymbol{U}^*_\alpha - \boldsymbol{U}_\alpha\right) = \boldsymbol{F}^*_\alpha - \boldsymbol{F}_\alpha \,, \tag{32}$$

where $\alpha = L$ or $\alpha = R$ for the left or right state, respectively. In this respect, $\boldsymbol{F}^*_{\rm L}$ and $\boldsymbol{F}^*_{\rm R}$ should be regarded as independent unknowns in the problem. Additionally, if the middle wave is taken to be a contact discontinuity, states and fluxes should also satisfy the jump conditions across it,

$$\lambda^* \left(\boldsymbol{U}^*_{\rm L} - \boldsymbol{U}^*_{\rm R}\right) = \boldsymbol{F}^*_{\rm L} - \boldsymbol{F}^*_{\rm R} \,, \tag{33}$$

by consistently demanding continuity of magnetic field, velocity, and total pressure across λ^*. Equation (32) may be replaced by two alternative sets derived by direct summation of the jump relations across all waves [31, 32, 33].

The first set yields the traditional consistency conditions [46] in terms of the state vectors $\boldsymbol{U}^*_{\rm L}$ and $\boldsymbol{U}^*_{\rm R}$,

$$\frac{(\lambda^* - \lambda_{\rm L})\boldsymbol{U}^*_{\rm L} + (\lambda_{\rm R} - \lambda^*)\boldsymbol{U}^*_{\rm R}}{\lambda_{\rm R} - \lambda_{\rm L}} = \boldsymbol{U}^{\rm hll} \,, \tag{34}$$

where $\boldsymbol{U}^{\rm hll}$ is given by Eq. (26). The second set, obtained after dividing each jump condition by the corresponding wave speed and adding the resulting expressions, yields a similar relation for the fluxes $\boldsymbol{F}^*_{\rm L}$ and $\boldsymbol{F}^*_{\rm R}$:

$$\frac{\boldsymbol{F}^*_{\rm L}\lambda_{\rm R}(\lambda^* - \lambda_{\rm L}) + \boldsymbol{F}^*_{\rm R}\lambda_{\rm L}(\lambda_{\rm R} - \lambda^*)}{\lambda_{\rm R} - \lambda_{\rm L}} = \lambda^* \boldsymbol{F}^{\rm hll} \,, \tag{35}$$

where $\boldsymbol{F}^{\rm hll}$ is given by Eq. (28).

The problem is well posed if the number of unknowns exactly matches the number of available equations. Considering the normal component of the magnetic field, B_x, as a constant parameter, one has at disposal a total of 21 equations: 14 for the outer waves $(7 + 7)$ and 7 from the jumps across the middle contact wave, Eq. (33). Since λ^* is unknown (it is not determined a priori), it follows that states and fluxes in the *star* region should be written in terms of 20 unknown variables, 10 per state. There is, however, some degree of freedom in choosing this representation.

Both Gurski [21] and Li [28] proposed to express the unknowns and fluxes in the *star* regions as

$$\boldsymbol{U}^*_\alpha = \begin{pmatrix} \rho^*_\alpha \\ \rho^*_\alpha \lambda^* \\ \rho^*_\alpha \boldsymbol{v}^*_{t_\alpha} \\ \boldsymbol{B}^*_{t_\alpha} \\ E^*_\alpha \end{pmatrix}, \quad \boldsymbol{F}^*_\alpha = \begin{pmatrix} \rho^*_\alpha \lambda^* \\ \rho^*_\alpha (\lambda^*)^2 + p^* - B_x^2 \\ \rho^*_\alpha \boldsymbol{v}^*_{t_\alpha} \lambda^* - B_x \boldsymbol{B}^*_{t_\alpha} \\ \boldsymbol{B}^*_{t_\alpha} \lambda^* - \boldsymbol{v}^*_{t_\alpha} B_x \\ (E^*_\alpha + p^*_\alpha)\lambda^* - B_x \left(\boldsymbol{B} \cdot \boldsymbol{v}\right)^*_\alpha \end{pmatrix}, \tag{36}$$

where $\alpha = L$ or $\alpha = R$ for the left or right state, respectively. In Eq. (36) the fluid normal velocity is assumed to be continuous across the contact mode and equal to the speed of the discontinuity itself, that is, $\lambda^* = u^*_{\rm L} = u^*_{\rm R}$. By exploiting the continuity of tangential magnetic field and total pressure across the contact (entropy) mode, one can easily find, from Eqs. (34) and (35), the *unique* choices

$$\lambda^* = \frac{m_x^{\rm hll}}{\rho^{\rm hll}}\,, \quad \boldsymbol{B}^*_{t_{\rm L}} = \boldsymbol{B}^*_{t_{\rm R}} = \boldsymbol{B}^{\rm hll}_t\,, \quad p^*_{\rm L} = p^*_{\rm R} = F^{\rm hll}_{[m_x]} + B_x^2 - F^{\rm hll}_{[\rho]}\lambda^*\,, \quad (37)$$

where $m_x^{\rm hll}$ and $\boldsymbol{B}^{\rm hll}_{t_\alpha}$ are, respectively, the normal momentum and transverse magnetic field components given by the HLL-averaged state $\boldsymbol{U}^{\rm hll}$, see Eq. (26).

In [28], the expressions for density and transverse components of momentum are derived from the jump conditions across the outermost waves, Eq. (32):

$$\rho^*_\alpha = \rho_\alpha \frac{\lambda_\alpha - u_\alpha}{\lambda_\alpha - \lambda^*}\,, \quad (\rho_\alpha \boldsymbol{v}_{t_\alpha})^* = \rho^*_\alpha \boldsymbol{v}_{t_\alpha} - B_x \frac{\boldsymbol{B}^*_{t_\alpha} - \boldsymbol{B}_{t_\alpha}}{\lambda_\alpha - \lambda^*}\,, \quad (38)$$

and similarly for the energy:

$$E^*_\alpha = \frac{E_\alpha(\lambda_\alpha - u_\alpha) + (p^*\lambda^* - p_\alpha u_\alpha) - B_x\left[(\boldsymbol{B}\cdot\boldsymbol{v})^*_\alpha - \boldsymbol{B}_\alpha\cdot\boldsymbol{v}_\alpha\right]}{\lambda_\alpha - \lambda^*}\,, \quad (39)$$

where, from the consistency condition, one must have $(\boldsymbol{B}\cdot\boldsymbol{v})^*_{\rm L} = (\boldsymbol{B}\cdot\boldsymbol{v})^*_{\rm R}$. Since $\boldsymbol{B}^*_{t{\rm L}} = \boldsymbol{B}^*_{t{\rm R}}$ is continuous across the middle wave, a possibility is to set $\boldsymbol{v}^* = \boldsymbol{m}^{\rm hll}/\rho^{\rm hll}$ as done in [28]. However, this choice is somewhat inconsistent with the expression of $\boldsymbol{v}^*_{t{\rm L}}$ and $\boldsymbol{v}^*_{t{\rm R}}$ recovered from the second equation in (38). Indeed, Li's formulation introduces only nine unknowns per state: $\rho^*, \lambda^*, \boldsymbol{v}^*_t, \boldsymbol{B}^*_t, E^*, p^*$, and $(\boldsymbol{v}\cdot\boldsymbol{B})^*$. As such, it has been derived by using 18 equations only, namely the 14 jumps across the outer waves, Eq. (32), together with the imposed continuity of u^*, $\boldsymbol{B}^*_t$, and p^*. Consequently, it fails to satisfy some of the jump relations across the middle wave as it can be verified from the components of the induction equation.

Similar inconsistencies can also be found in [21], which defines both normal and tangential velocities as ratios between HLL-averaged momentum and density, i.e., $\boldsymbol{v}^*_{\rm L} \equiv \boldsymbol{v}^*_{\rm R} = \boldsymbol{m}^{\rm hll}/\rho^{\rm hll}$. In a second derivation, in the attempt to gain further benefits from the introduction of the middle wave (such as capturing isolated slow or Alfvén waves), Gurski [21] relaxes the assumption of continuity in the transverse component of $\boldsymbol{v}$ and $\boldsymbol{B}$. The resulting $\boldsymbol{U}^*_{\rm L}$ and $\boldsymbol{U}^*_{\rm R}$ derived in this way do not satisfy the jump conditions. This freedom comes at the extra cost of introducing a dissipation terms to control unwanted spurious numerical oscillations.

A consistent formulation may be derived by following [32], who extended the HLLC formalism to the equations of relativistic MHD. Since one must have 10 unknowns per state, the following expressions can be introduced

$$\boldsymbol{U}^*_\alpha = \begin{pmatrix} \rho^*_\alpha \\ \rho^*_\alpha \lambda^* \\ \boldsymbol{m}^*_{t_\alpha} \\ \boldsymbol{B}^*_{t_\alpha} \\ E^*_\alpha \end{pmatrix}, \quad \boldsymbol{F}^*_\alpha = \begin{pmatrix} \rho^*_\alpha \lambda^* \\ \rho^*_\alpha (\lambda^*)^2 + p^* - B_x^2 \\ \boldsymbol{m}^*_{t_\alpha} \lambda^* - B_x \boldsymbol{B}^*_{t_\alpha} \\ \boldsymbol{B}^*_{t_\alpha} \lambda^* - \boldsymbol{v}^*_{t_\alpha} B_x \\ (E^*_\alpha + p^*_\alpha)\lambda^* - B_x \left(\boldsymbol{B}\cdot\boldsymbol{v}\right)^*_\alpha \end{pmatrix}, \tag{40}$$

where $\boldsymbol{m}^*_{t_\alpha}$ is the transverse momentum. One must realize that, for the sake of consistency, one has to assume $\rho^*_\alpha \boldsymbol{v}^*_{t_\alpha} \neq \boldsymbol{m}^*_{t_\alpha}$ in the previous equations, although one still has $m^*_{x_\alpha} = \rho^*_\alpha \lambda^*$. This comes from the fact that the average momentum is not simply equal to the average density times the average velocity. Note that the proposed formulation is not necessarily unique; for example, there is some degree of freedom in writing term $(\boldsymbol{v}\cdot\boldsymbol{B})^*$ in the energy flux as $\boldsymbol{v}^*\cdot\boldsymbol{B}^*$ or $\boldsymbol{m}^*\cdot\boldsymbol{B}^*/\rho^*$. Nevertheless, the advantage offered by the previous expressions is the introduction of 10 unknowns per state, complemented by 14 equations across the outer fast shocks and six additional constraints imposed through the entropy mode:

$$[p^*] = [\lambda^*] = [\boldsymbol{B}^*_{t_\alpha}] = [\boldsymbol{v}^*_{t_\alpha}] = 0\,. \tag{41}$$

As for Li's solver, this leads to the unique choices given by Eq. (37). However, although the first equation for ρ^*_α in (38) still holds, the second one should be replaced by:

$$\boldsymbol{m}^*_{t_\alpha} = \boldsymbol{m}_{t_\alpha} \frac{\lambda_\alpha - u_\alpha}{\lambda_\alpha - \lambda^*} + B_x \frac{\boldsymbol{B}_{t_\alpha} - \boldsymbol{B}^*_{t_\alpha}}{\lambda_\alpha - \lambda^*}\,. \tag{42}$$

Having defined the magnetic field, the velocities can be derived directly from Eq. (35),

$$\boldsymbol{v}^*_{t_\alpha} = \frac{\boldsymbol{B}^*_{t_\alpha}\lambda^* - \boldsymbol{F}^{\rm hll}_{B_{t\alpha}}}{B_x}\,, \tag{43}$$

which may become ill defined as $B_x \to 0$. However this is not the case here, since what really matters in the induction and energy fluxes in Eq. (40) is $B_x \boldsymbol{v}^*_{t_\alpha}$ rather than the transverse velocity. Finally, the energy can be obtained from Eq. (39) by using either $\boldsymbol{v}^*\cdot\boldsymbol{B}^*$ or $\boldsymbol{m}^*\cdot\boldsymbol{B}^*/\rho^*$.

The Multi state HLL Solver: HLLD

The formulation adopted by Miyoshi and Kusano [35] solves the apparent incompatibilities introduced by the HLLC approach. The "HLLD solver" ("D" stands for "discontinuity"), introduced by [35], approximates the structure of the Riemann fan introducing five waves corresponding to two outermost fast shocks ($\lambda_{\rm L}$ and $\lambda_{\rm R}$) and two rotational discontinuities ($\lambda^*_{\rm L}$ and $\lambda^*_{\rm R}$) separated by a contact mode in the middle (λ^*_c). The resulting structure comprises four states, $\boldsymbol{U}^*_{\rm L}$, $\boldsymbol{U}^{**}_{\rm L}$, $\boldsymbol{U}^{**}_{\rm R}$, and $\boldsymbol{U}^*_{\rm R}$ as shown in Fig. 6. Across the rotational waves, density, total pressure, and the normal component of velocity remain

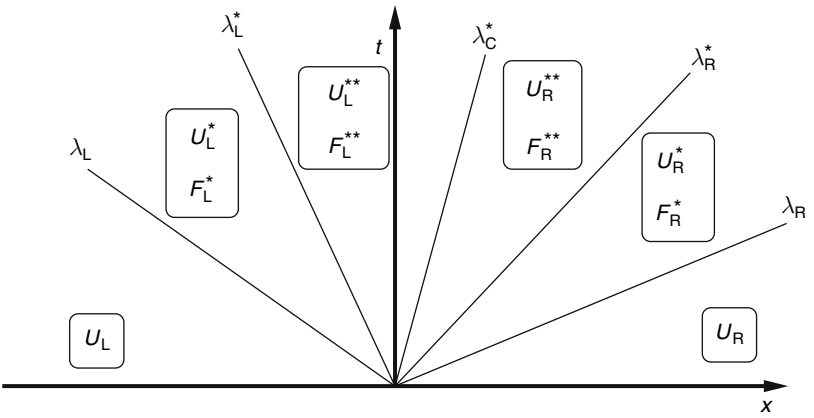

Fig. 6. Approximate structure to the Riemann fan used by the HLLD solver. Five waves separating four states are adopted. The *outermost waves* $\lambda_{\rm L}$ and $\lambda_{\rm R}$ correspond to fast shocks, while $\lambda_{\rm L}^*$ and $\lambda_{\rm R}^*$ identify rotational discontinuity. The *central wave* $\lambda_{\rm c}^*$ is the entropy mode

continuous. On the other hand, one must conserve $\boldsymbol{B}_t$, $\boldsymbol{v}$, and total pressure p through the contact mode. Since slow modes are not allowed inside the structure, p and u can be assumed constant throughout the Riemann fan and the normal velocity corresponds to the speed of the middle (entropy) wave. State and flux vectors retain the representation given by Eq. (36) in terms of eight unknown quantities in each state: $\rho^*, \lambda^*, \boldsymbol{v}_t^*, \boldsymbol{B}_t^*, E^*$, and p^*. As shown below, this formulation leads to a well-posed problem.

As a starting point, one can conveniently extend the derivation of the consistency conditions (34) and (35) to

$$\frac{(\lambda_{\rm R}-\lambda_{\rm R}^*)\,\boldsymbol{U}_{\rm R}^* + (\lambda_{\rm R}^*-\lambda_c^*)\,\boldsymbol{U}_{\rm R}^{**} + (\lambda_c^*-\lambda_{\rm L}^*)\,\boldsymbol{U}_{\rm L}^{**} + (\lambda_{\rm L}^*-\lambda_{\rm L})\,\boldsymbol{U}_{\rm L}^*}{\lambda_{\rm R}-\lambda_{\rm L}} = \boldsymbol{U}^{\rm hll}\,, \tag{44}$$

and, setting $\eta = 1/\lambda$,

$$\frac{(\eta_{\rm R}-\eta_{\rm R}^*)\,\boldsymbol{F}_{\rm R}^* + (\eta_{\rm R}^*-\eta_c^*)\,\boldsymbol{F}_{\rm R}^{**} + (\eta_c^*-\eta_{\rm L}^*)\,\boldsymbol{F}_{\rm L}^{**} + (\eta_{\rm L}^*-\eta_{\rm L})\,\boldsymbol{F}_{\rm L}^*}{\eta_{\rm R}-\eta_{\rm L}} = \boldsymbol{F}^{\rm hll}\,. \tag{45}$$

Since $\rho_\alpha^* = \rho_\alpha^{**}$, the density and momentum components of (44) yield the obvious choice

$$\lambda_c^* \equiv u_{\rm L}^* = u_{\rm L}^{**} = u_{\rm R}^{**} = u_{\rm R}^* = \frac{m_x^{\rm hll}}{\rho^{\rm hll}}\,. \tag{46}$$

Likewise, using the same components in Eq. (44) one has

$$p^* \equiv p_{\rm L}^* = p_{\rm L}^{**} = p_{\rm R}^{**} = p_{\rm R}^* = F_{[m_x]}^{\rm hll} + B_x^2 - F_{[\rho]}^{\rm hll}\lambda_c^*\,. \tag{47}$$

The jump conditions across the outermost waves can now be used to determine the flow variables in the *star* regions as

$$\rho^*_\alpha = \rho_\alpha \frac{\lambda_\alpha - u_\alpha}{\lambda_\alpha - \lambda^*_c}\,, \tag{48}$$

$$\boldsymbol{B}^*_{t_\alpha} = \boldsymbol{B}_{t_\alpha} \frac{\rho_\alpha \left(\lambda_\alpha - u_\alpha\right)^2 - B_x^2}{\rho_\alpha(\lambda_\alpha - u_\alpha)(\lambda_\alpha - \lambda^*_c) - B_x^2}\,, \tag{49}$$

$$\boldsymbol{v}^*_{t_\alpha} = \boldsymbol{v}_{t_\alpha} - B_x \frac{\boldsymbol{B}^*_{t_\alpha} - \boldsymbol{B}_{t_\alpha}}{\rho_\alpha(\lambda_\alpha - u_\alpha)}\,, \tag{50}$$

$$E^*_\alpha = \frac{(\lambda_\alpha - u_\alpha)\, E_\alpha - p_\alpha u_\alpha + p^* \lambda^*_c + B_x \left(\boldsymbol{v}_\alpha \cdot \boldsymbol{B}_\alpha - \boldsymbol{v}^*_\alpha \cdot \boldsymbol{B}^*_\alpha\right)}{\lambda_\alpha - \lambda^*_c}\,, \tag{51}$$

where $\alpha = L$ or $\alpha = R$ for the left or right state, respectively.

The jump conditions across the rotational modes $\lambda^*_{\rm L}$ and $\lambda^*_{\rm R}$,

$$\lambda^*_\alpha \left(\boldsymbol{U}^{**}_\alpha - \boldsymbol{U}^*_\alpha\right) = \boldsymbol{F}^{**}_\alpha - \boldsymbol{F}_\alpha\,, \tag{52}$$

cannot be solved independently to satisfy $\boldsymbol{B}^{**}_{t\rm L} = \boldsymbol{B}^{**}_{t\rm R}$ and $\boldsymbol{v}^{**}_{t\rm L} = \boldsymbol{v}^{**}_{t\rm R}$, unless the equations are linearly dependent. Indeed, only two out of the four relations for the transverse vector fields (for each wave) can be regarded independent, provided the speeds of the discontinuities are chosen to satisfy

$$\lambda^*_{\rm L} = \lambda^*_c - \frac{|B_x|}{\sqrt{\rho^*_{\rm L}}}\,, \quad \lambda^*_{\rm R} = \lambda^*_c + \frac{|B_x|}{\sqrt{\rho^*_{\rm R}}}\,. \tag{53}$$

The consistency condition (44) can now be used to find the state variables on either side of the entropy wave:

$$\boldsymbol{v}^{**}_{t_{\rm L}} = \boldsymbol{v}^{**}_{t_{\rm R}} = \frac{\sqrt{\rho^*_{\rm L}}\boldsymbol{v}^*_{t_{\rm L}} + \sqrt{\rho^*_{\rm R}}\boldsymbol{v}^*_{t_{\rm R}} + \left(\boldsymbol{B}_{t_{\rm R}} - \boldsymbol{B}_{t_{\rm L}}\right)\sigma_x}{\sqrt{\rho^*_{\rm L}} + \sqrt{\rho^*_{\rm R}}}\,, \tag{54}$$

$$\boldsymbol{B}^{**}_{t_{\rm L}} = \boldsymbol{B}^{**}_{t_{\rm R}} = \frac{\sqrt{\rho^*_{\rm L}}\boldsymbol{B}^*_{t_{\rm R}} + \sqrt{\rho^*_{\rm R}}\boldsymbol{B}^*_{t_{\rm L}} + \sqrt{\rho^*_{\rm L}\rho^*_{\rm R}}\left(\boldsymbol{v}_{t_{\rm R}} - \boldsymbol{v}_{t_{\rm L}}\right)\sigma_x}{\sqrt{\rho^*_{\rm R}} + \sqrt{\rho^*_{\rm L}}}\,, \tag{55}$$

with $\sigma_x = \mathrm{sign}(B_x)$. For the energy one finds

$$E^{**}_{\rm L} = E^*_{\rm L} - \sqrt{\rho^*_{\rm L}}\left(\boldsymbol{v}^*_{\rm L} \cdot \boldsymbol{B}^*_{\rm L} - \boldsymbol{v}^{**}_{\rm L} \cdot \boldsymbol{B}^{**}_{\rm L}\right)\sigma_x\,, \tag{56}$$

$$E^{**}_{\rm R} = E^*_{\rm R} + \sqrt{\rho^*_{\rm R}}\left(\boldsymbol{v}^*_{\rm R} \cdot \boldsymbol{B}^*_{\rm R} - \boldsymbol{v}^{**}_{\rm R} \cdot \boldsymbol{B}^{**}_{\rm R}\right)\sigma_x\,. \tag{57}$$

As one can see, the problem is defined in terms of 32 unknowns (eight per state) complemented by 32 independent non trivial equations: 14 across the outermost waves (seven for $\alpha = L$ and seven for $\alpha = R$), six continuity conditions across the contact mode:

$$[p] = [u] = 0\,, \quad [\boldsymbol{B}_t] = [\boldsymbol{v}_t] = \boldsymbol{0}\,, \tag{58}$$

and 12 conditions across the rotational waves, six of which are given by

$$[\rho] = [u] = [p] = 0\,, \tag{59}$$

(across $\lambda_{\rm L}^*$ and $\lambda_{\rm R}^*$), plus six *independent* jump conditions for $\boldsymbol{B}_t$, $\boldsymbol{v}_t$, and E.

It is now straightforward to compute the inter cell numerical flux:

$$\hat{\boldsymbol{f}} = \begin{cases} \boldsymbol{F}_{\rm L} & \text{if} \quad \lambda_{\rm L} \geq 0, \\ \boldsymbol{F}_{\rm L}^* & \text{if} \quad \lambda_{\rm L} \leq 0 \leq \lambda_{\rm L}^*\,, \\ \boldsymbol{F}_{\rm L}^{**} & \text{if} \quad \lambda_{\rm L}^* \leq 0 \leq \lambda_c^*\,, \\ \boldsymbol{F}_{\rm R}^{**} & \text{if} \quad \lambda_c^* \leq 0 \leq \lambda_{\rm R}^*\,, \\ \boldsymbol{F}_{\rm R}^* & \text{if} \quad \lambda_{\rm R}^* \leq 0 \leq \lambda_{\rm R}\,, \\ \boldsymbol{F}_{\rm R} & \text{if} \quad \lambda_{\rm R} \leq 0\,. \end{cases} \tag{60}$$

The HLLD flux is found to be robust with an accuracy comparable to that of the Roe scheme. Recently, [33], this methodology has been extended to the isothermal MHD equations.

The Scheme of Roe

Roe's scheme [39] tries to resolve the initial jump by replacing the original conservation law with a linearized system of constant coefficients. Thus one proceeds by seeking the exact solution to the following linearized Riemann problem:

$$\begin{cases} \dfrac{\partial \boldsymbol{U}}{\partial t} + \overline{\boldsymbol{A}}_{\rm LR} \cdot \dfrac{\partial \boldsymbol{U}}{\partial x} = \boldsymbol{0}, \\ \boldsymbol{U}(x,0) = \begin{cases} \boldsymbol{U}_{\rm L} & \text{for} \quad x < 0, \\ \boldsymbol{U}_{\rm R} & \text{for} \quad x > 0. \end{cases} \end{cases} \tag{61}$$

where $\overline{\boldsymbol{A}}_{\rm RL} \equiv \overline{\boldsymbol{A}}(\boldsymbol{U}_{\rm L}, \boldsymbol{U}_{\rm R})$ is a constant matrix. The matrix $\overline{\boldsymbol{A}}_{\rm LR}$ is called a Roe matrix if the following requirements are met [46]:

- Consistency with the original conservation law: $\overline{\boldsymbol{A}}(\boldsymbol{U}, \boldsymbol{U}) = \boldsymbol{A}(\boldsymbol{U})$, where $\boldsymbol{A}$ is simply the jacobian of the flux, i.e., $\boldsymbol{A}\,(\boldsymbol{U}) = \partial \boldsymbol{F}(\boldsymbol{U})/\partial \boldsymbol{U}$
- Conservation across discontinuities:

$$\boldsymbol{F}\,(\boldsymbol{U}_{\rm R}) - \boldsymbol{F}\,(\boldsymbol{U}_{\rm L}) = \overline{\boldsymbol{A}}_{\rm LR} \cdot (\boldsymbol{U}_{\rm R} - \boldsymbol{U}_{\rm L})\,. \tag{62}$$

- Hyperbolicity: $\overline{\boldsymbol{A}}$ must have a complete set of real eigenvalues $\lambda_k(\boldsymbol{U}_{\rm L}, \boldsymbol{U}_{\rm R})$ and associated left and right eigenvectors $\boldsymbol{L}_k$ and $\boldsymbol{R}_k$ such that

$$\boldsymbol{A} \cdot \boldsymbol{R}_k = \lambda_k \boldsymbol{R}_k, \quad \boldsymbol{L}_k \cdot \boldsymbol{A} = \lambda_k \boldsymbol{L}_k. \tag{63}$$

Roe's scheme is thus equivalent to the solution of the Riemann problem for a system of advection equation with linear constant coefficients, for which the flux function takes the form:

$$\hat{\boldsymbol{f}} = \frac{\boldsymbol{F}_{\rm L} + \boldsymbol{F}_{\rm R}}{2} - \frac{1}{2}\sum_k \left(\boldsymbol{L}_k \cdot \Delta\boldsymbol{U}\right) |\lambda_k| \boldsymbol{R}_k, \tag{64}$$

and $\Delta\boldsymbol{U} = \boldsymbol{U}_{\rm R} - \boldsymbol{U}_{\rm L}$. Despite the original method of Roe, initially developed for the Euler equation of gasdynamics, has been extended to MHD using simpler averages (e.g., the arithmetic average, see for example [5, 37, 42, 44], Cargo and Gallice [6] showed how the correct Roe matrix for MHD can be constructed for any value of the specific heat ratio Γ. For the sake of completeness, we report hereafter the expressions. To this purpose, we introduce two different Roe averages for any flow quantity Q by defining

$$\overline{Q} = \frac{\sqrt{\rho_{\rm L}} Q_{\rm L} + \sqrt{\rho_{\rm R}} Q_{\rm R}}{\sqrt{\rho_{\rm L}} + \sqrt{\rho_{\rm R}}}\,, \quad \underline{Q} = \frac{\sqrt{\rho_{\rm R}} Q_{\rm L} + \sqrt{\rho_{\rm L}} Q_{\rm R}}{\sqrt{\rho_{\rm L}} + \sqrt{\rho_{\rm R}}}\,. \tag{65}$$

Velocity and specific enthalpy $H = (E + p)/\rho$ are computed using the first definition, whereas density and transverse components of the field follow the second one. In other words, $\boldsymbol{v}, H \in \overline{Q}$, while $\rho, \boldsymbol{B}_t \in \underline{Q}$. Next we compute the jumps in conservative variables, that is, $\Delta\boldsymbol{U} = \boldsymbol{U}_{\rm R} - \boldsymbol{U}_{\rm L}$. The pressure jump is derived accordingly as

$$\Delta p = (\Gamma - 1)\left[\left(\frac{\boldsymbol{v}^2}{2} - X\right)\Delta\rho - \boldsymbol{v}\cdot\Delta\left(\rho\boldsymbol{v}\right) + \Delta E - \boldsymbol{B}\cdot\Delta\boldsymbol{B}\right], \tag{66}$$

with

$$X = \frac{\Delta\boldsymbol{B}\cdot\Delta\boldsymbol{B}}{2\left(\sqrt{\rho_{\rm L}} + \sqrt{\rho_{\rm R}}\right)^2}\,. \tag{67}$$

Now, according to the chosen set of variables, we compute the sound speed a and Alfvén velocity $c_{\rm A}$ as

$$a^2 = (2 - \Gamma)X + (\Gamma - 1)\left(H - \frac{\boldsymbol{v}^2}{2} - \frac{\boldsymbol{B}^2}{\rho}\right), \quad c_{\rm A}^2 = \frac{B_x^2}{\rho}\,, \tag{68}$$

while fast and slow velocities $c_{\rm f}$ and $c_{\rm s}$ are given by

$$c_{\rm f}^2 = \frac{1}{2}\left(a^2 + \frac{\boldsymbol{B}^2}{\rho} + \sqrt{\left(a^2 - b^2\right)^2 + 4\boldsymbol{b}_t^2 a^2}\right), \quad c_{\rm s}^2 = \frac{a^2 c_A^2}{c_{\rm f}^2}\,. \tag{69}$$

Having defined the Roe average, we now give the expressions for the right eigenvectors $\boldsymbol{R}_k$ and wave strengths $\boldsymbol{L}_k\cdot\Delta\boldsymbol{U}$ required in Eq. (64). For convenience, we define [6]

$$\alpha_f = \frac{a^2 - c_s^2}{c_f^2 - c_s^2}\,, \quad \alpha_s = \frac{c_f^2 - a^2}{c_f^2 - c_s^2}\,, \quad S_s = \alpha_s c_s \sigma_x\,, \quad S_f = \alpha_f c_f \sigma_x\,, \tag{70}$$

where $\sigma_x = \mathrm{sign}(B_x)$. The right eigenvectors for the fast modes $f\pm$ with eigenvalues $\lambda_{f\pm} = u \pm c_f$ are

$$\boldsymbol{R}_{f\pm} = \begin{pmatrix} \alpha_f \\ \alpha_f \lambda_{f\pm} \\ (\alpha_f \boldsymbol{v}_t \mp S_s \boldsymbol{\beta}_t) \\ \dfrac{\alpha_s}{\sqrt{\rho}} a \boldsymbol{\beta}_t \\ \alpha_f \left(H^* - \dfrac{\boldsymbol{B}^2}{\rho} \pm v_x c_f \right) \mp S_s \left(\boldsymbol{v}_t \cdot \boldsymbol{\beta}_t \right) + \dfrac{\alpha_s}{\sqrt{\rho}} a \left| \boldsymbol{B}_t \right| \end{pmatrix} . \tag{71}$$

Similarly, the expressions for the slow modes $s\pm$ associated with $\lambda_{s\pm} = u \pm c_s$ follow:

$$\boldsymbol{R}_{s\pm} = \begin{pmatrix} \alpha_s \\ \alpha_s \lambda_{s\pm} \\ (\alpha_s \boldsymbol{v}_t \pm S_f \boldsymbol{\beta}_t) \\ -\dfrac{\alpha_f}{\sqrt{\rho}} a \boldsymbol{\beta}_t \\ \alpha_s \left(H^* - \dfrac{\boldsymbol{B}^2}{\rho} \pm v_x c_s \right) \pm S_f \left(\boldsymbol{v}_t \cdot \boldsymbol{\beta}_t \right) - \dfrac{\alpha_f}{\sqrt{\rho}} a \left| \boldsymbol{B}_t \right| \end{pmatrix} . \tag{72}$$

The linear modes are given by the rotational Alfvén waves propagating at $\lambda_{A\pm} = u \pm c_A$ and the entropy contact mode moving at the flow velocity $\lambda_u = u$. The associated expressions for the corresponding right eigenvectors are found to be

$$\boldsymbol{R}_u = \begin{pmatrix} 1 \\ u \\ \boldsymbol{v}_t \\ \boldsymbol{0} \\ \dfrac{\boldsymbol{v}^2}{2} + \dfrac{\Gamma - 2}{\Gamma - 1} X \end{pmatrix} , \quad \boldsymbol{R}_{A\pm} = \begin{pmatrix} 0 \\ 0 \\ \pm \rho \boldsymbol{\beta}_t \times \hat{\boldsymbol{n}} \\ -S \sqrt{\rho} \boldsymbol{\beta}_t \times \hat{\boldsymbol{n}} \\ \pm \rho \left(\boldsymbol{v}_t \times \boldsymbol{\beta}_t \cdot \hat{\boldsymbol{n}} \right) \end{pmatrix} . \tag{73}$$

We conclude the presentation by providing the expressions for the wave strengths:

$$\boldsymbol{L}_{f\pm} \cdot \Delta \boldsymbol{U} = \frac{\alpha_f Y \mp \rho S_s \boldsymbol{\beta}_t \cdot \Delta \boldsymbol{v}_t \pm \rho \alpha_f c_f \Delta u + \sqrt{\rho} \alpha_s a \boldsymbol{\beta}_t \cdot \Delta \boldsymbol{B}_t}{2a^2} , \tag{74}$$

$$\boldsymbol{L}_{s\pm} \cdot \Delta \boldsymbol{U} = \frac{\alpha_s Y \pm \rho S_f \boldsymbol{\beta}_t \cdot \Delta \boldsymbol{v}_t \pm \rho \alpha_s c_s \Delta u - \sqrt{\rho} \alpha_f a \boldsymbol{\beta}_t \cdot \Delta \boldsymbol{B}_t}{2a^2} , \tag{75}$$

and

$$\boldsymbol{L}_{A\pm} \cdot \Delta \boldsymbol{U} = \frac{\boldsymbol{\beta}_t}{2} \times \left[\mp \Delta \boldsymbol{v} + \frac{S}{\sqrt{\rho}} \Delta \boldsymbol{B}_t \right] \cdot \hat{\boldsymbol{n}} , \quad \boldsymbol{L}_u \cdot \Delta \boldsymbol{U} = 1 - \frac{Y}{a^2} , \tag{76}$$

where $Y = (X\Delta\rho + \Delta p)$, and $\hat{\boldsymbol{n}}$ is the unit vector normal to the discontinuity front.

The Riemann solver of Roe is able to correctly capture any isolated regular discontinuity, including fast, slow, Alfvén, and contact fronts. In some circumstances, however, the Roe solver can fail giving rise to unphysical (negative) pressures or trigger spurious numerical instabilities, such as the *carbuncle* phenomenon, [38]. Also, the assumption of strict hyperbolicity ceases when some of the eigenvectors are not linearly independent anymore, [40]. For this reason, regions of the flow that might potentially cause problems are treated with an hybrid Riemann solver that selectively switch from Roe's scheme to a more robust (albeit less accurate) scheme such as HLL.

4 The $\nabla \cdot \boldsymbol{B} = 0$ Condition

The absence of magnetic monopoles is mathematically expressed by Gauss' law for magnetism, i.e.,

$$\nabla \cdot \boldsymbol{B} = 0\,, \tag{77}$$

which simply states that, for any control volume, the net magnetic flux across the boundary is identically zero. In other words, magnetic fields do not have sink or sources. The solenoidal condition is not an evolutionary equation but, rather, a constraint to be fulfilled at all times. Indeed, if $\nabla \cdot \boldsymbol{B} = 0$ at some initial time, then by taking the divergence of Faraday's law of electromagnetism

$$\frac{\partial \boldsymbol{B}}{\partial t} + \nabla \times \boldsymbol{\Omega} = 0\,, \tag{78}$$

one has $\partial \nabla \cdot \boldsymbol{B}/\partial t = 0$, i.e., the field is divergence-free at all times.

From a numerical point of view, however, this condition is fulfilled only at the truncation level and non solenoidal components may be generated during the evolution. This causes unphysical accelerations of the plasma in the direction parallel to the field lines, as outlined by [4]. Generally speaking, it is not possible for a numerical scheme to satisfy $\nabla \cdot \boldsymbol{B} = 0$ for any type of discretization. Thus different method of solutions can be sought and the robustness of one strategy over another can be established on a practical base by extensive numerical testing. In what follows, we give a rather concise description of the different approaches embraced up to now in Godunov type schemes, and follow a two-category classification.

In the first one, a cell-centered representation of the magnetic field is used. This naturally extends the formalism developed for the Euler equation of gasdynamics to MHD and offers the advantage of being conceptually simple and easy to implement in existing hydrocodes. Moreover, exploiting a cell-centered representation of all conserved quantities makes the extension to adaptive and unstructured grids straightforward.

In the second class, the magnetic field has a staggered representation whereby field components live on the face they are normal to. Hydrodynamics variables (density, velocity, and pressure) retains their usual collocation at the cell center. This provides a framework by which the induction equation (78) is more naturally updated using Stoke's theorem and the divergence-free condition is fulfilled to machine accuracy, if $\nabla \cdot \boldsymbol{B} = 0$ initially.

4.1 Cell-Centered Methods

Powell's 8-Wave Formulation

In the 8-wave formulation [36], Gauss' law for magnetism is discarded in the physical derivation of the MHD equations [37]. From the vector identity

$$\nabla \times (\boldsymbol{v} \times \boldsymbol{B}) = \boldsymbol{v}\,(\nabla \cdot \boldsymbol{B}) - \boldsymbol{B}\,(\nabla \cdot \boldsymbol{v}) + (\boldsymbol{v} \cdot \nabla)\,\boldsymbol{B} - (\boldsymbol{v} \cdot \nabla)\,\boldsymbol{B}\,, \tag{79}$$

and the fact that $\nabla \cdot (\boldsymbol{vB}) = (\nabla \cdot \boldsymbol{v})\boldsymbol{B} + (\boldsymbol{v} \cdot \nabla)\boldsymbol{B}$, one can re write Fraday's law as

$$\frac{\partial \boldsymbol{B}}{\partial t} + \nabla \cdot (\boldsymbol{vB} - \boldsymbol{Bv}) = -\boldsymbol{v}\,(\nabla \cdot \boldsymbol{B})\ . \tag{80}$$

Likewise, applying the same arguments to the momentum equation

$$\frac{\partial(\rho \boldsymbol{v})}{\partial t} + \nabla \cdot [\rho \boldsymbol{vv} + p_g \boldsymbol{I}] = \boldsymbol{j} \times \boldsymbol{B} \quad \text{with} \quad \boldsymbol{j} = \nabla \times \boldsymbol{B}\,, \tag{81}$$

and to the energy equation

$$\frac{\partial}{\partial t}\left(\rho\epsilon + \rho\frac{\boldsymbol{v}^2}{2}\right) + \nabla \cdot \left[\left(\rho\epsilon + p_g + \rho\frac{\boldsymbol{v}^2}{2}\right)\boldsymbol{v}\right] = \boldsymbol{j} \cdot \boldsymbol{B}\,, \tag{82}$$

the divergence form of the equation takes the form [36, 37]

$$\frac{\partial}{\partial t}\begin{pmatrix} \rho \\ \rho\boldsymbol{v} \\ \boldsymbol{B} \\ E \end{pmatrix} + \nabla \cdot \begin{bmatrix} \rho\boldsymbol{v} \\ \rho\boldsymbol{vv} - \boldsymbol{BB} + p\boldsymbol{I} \\ \boldsymbol{vB} - \boldsymbol{Bv} \\ (E+p)\,\boldsymbol{v} - (\boldsymbol{v}\cdot\boldsymbol{B})\,\boldsymbol{B} \end{bmatrix} = -\nabla \cdot \boldsymbol{B} \begin{pmatrix} 0 \\ \boldsymbol{B} \\ \boldsymbol{v} \\ \boldsymbol{v}\cdot\boldsymbol{B} \end{pmatrix}, \tag{83}$$

where $p = p_g + \boldsymbol{B}^2/2$ is the total (thermal + magnetic) pressure and $E = \rho\epsilon + \rho\boldsymbol{v}^2/2 + \boldsymbol{B}^2/2$ is the total energy density.

Although the source term should be physically zero, Powell showed that its inclusion changes the character of the equations by introducing an additional eighth wave corresponding to the propagation of jumps in the component of magnetic field normal (B_x) to a given interface. The other seven waves are left unchanged from the traditional formulation, since it can be shown that none of them carries a jump in B_x.

The 8-wave formulation leads to a symmetrizable form of conservation laws which, among other properties [20, 23], makes the system Galilean invariant. This property does not hold anymore if the source term is dropped. Powell also showed that the 8-wave formulation leads to the passive advection of $(\nabla \cdot \boldsymbol{B})/\rho$. The latter property states that magnetic monopoles are advected by the flow as they are created. However, $\nabla \cdot \boldsymbol{B} = 0$ is not satisfied in any particular discretization, but only to truncation level.

Powell's method has the advantage of being computationally inexpensive and easy to implement without introducing significative complexities. Numerical tests show that this modification, in any existing shock-capturing MHD code, results in stable and robust schemes. On the other hand, the 8-wave formulation leads to a non conservative form of the equations. Although Powell claimed that deviations from the conservation should be very small, in [48] Tóth proved that near discontinuities (shock waves) large conservation errors may be produced.

Divergence Cleaning

In [12], the divergence free constraint is enforced by solving a modified system of conservation laws, where the induction equation is coupled to a generalized Lagrange multiplier. According to this modification, the induction equation is replaced with

$$\frac{\partial \boldsymbol{B}}{\partial t} + \nabla \cdot (\boldsymbol{v}\boldsymbol{B} - \boldsymbol{B}\boldsymbol{v}) + \nabla\psi = 0\,, \tag{84}$$

and the solenoidal condition is expressed through

$$\mathcal{D}(\psi) + \nabla \cdot \boldsymbol{B} = 0\,, \tag{85}$$

where $\mathcal{D}$ is a differential operator. For any choice of $\mathcal{D}$, one can show that the divergence of $\boldsymbol{B}$ and the scalar function ψ satisfy the same equation, namely

$$\frac{\partial}{\partial t}\mathcal{D}\left(\nabla \cdot \boldsymbol{B}\right) - \triangle\left(\nabla \cdot \boldsymbol{B}\right) = 0 \quad \Longleftrightarrow \quad \frac{\partial \mathcal{D}(\psi)}{\partial t} - \triangle\psi = 0\,. \tag{86}$$

An *elliptic* correction results from taking $\mathcal{D} = 0$. This is equivalent to the projection method introduced by [4] and explained in the next section.

By taking $\mathcal{D}(\psi) = \psi/c_p^2$ with $c_p > 0$, one ends up with a *parabolic* correction. Simple manipulations show that, in this case, ψ can be trivially eliminated from the equations and the induction equation becomes

$$\frac{\partial \boldsymbol{B}}{\partial t} + \nabla \cdot (\boldsymbol{v}\boldsymbol{B} - \boldsymbol{B}\boldsymbol{v}) = c_p^2 \nabla\left(\nabla \cdot \boldsymbol{B}\right)\,, \tag{87}$$

which states that local divergence errors are damped by an additional dissipation mechanism, provided compatible boundary conditions are used.

A third, *hyperbolic* correction follows if $\mathcal{D}(\psi) = c_h^{-2}\partial\psi/\partial t$ is chosen, with $c_h > 0$. The hyperbolic correction propagates local divergence errors to the boundary with the finite speed c_h.

Finally, a mixed hyperbolic/parabolic correction can be prescribed by summing up the respective differential operators. The resulting divergence constrain becomes

$$\frac{\partial \psi}{\partial t} + c_h^2 \nabla \cdot \boldsymbol{B} = -\frac{c_h^2}{c_p^2}\psi\,, \tag{88}$$

offering both dissipation and propagation of divergence errors. In the mixed formulation, divergence errors are transported to the domain boundaries with the maximal admissible speed and are damped at the same time.

The main advantage of the approaches outlined above and, in particular of the mixed formulation, is to preserve the full conservation form of the original MHD system. Indeed, only the equation for the unphysical scalar function ψ contains a source term. In addition, divergence errors are transported by two waves with speeds independent of the fluid velocity. In this respect, this procedure may be viewed as an extension of Powell's divergence wave. Finally, by taking advantage of operator splitting techniques, the equation for the normal component of the magnetic field and ψ are decoupled from the other equations. This allows for the solution of a 2×2 linear system of hyperbolic equations, thus considerably reducing the computational effort.

Projection Scheme

The projection scheme, originally proposed by Brackbill and Barnes [4], consists in applying a correction step to the magnetic field $\boldsymbol{B}^*$ obtained after the base scheme evolution (i.e., without any correction). In general, since the base scheme will not preserve the divergence free condition, one can use Helmholtz decomposition to resolve $\boldsymbol{B}^*$ as the sum of an irrotational and a solenoidal vector field, associated with scalar and vector potentials φ and $\boldsymbol{A}$, respectively:

$$\boldsymbol{B}^* = \nabla\varphi + \nabla \times \boldsymbol{A}\,. \tag{89}$$

The physically relevant part of the field is the one associated with the vector potential, i.e., $\nabla \times \boldsymbol{A}$. The correct divergence-free magnetic field is recovered by subtracting the unphysical contribution coming from the irrotational component, i.e.,

$$\boldsymbol{B}^{\rm new} = \boldsymbol{B}^* - \nabla\varphi\,, \tag{90}$$

after the Poisson equation

$$\nabla^2\varphi = \nabla \cdot \boldsymbol{B}^*\,, \tag{91}$$

obtained by taking the divergence of Eq. (89), has been solved. As noticed by Tóth [48], the difference operators approximating the divergence and gradient in Eqs. (90) and (91) must be consistently used to compute the Laplacian operator in the Poisson equation. He also proved that the correction given by Eq. (91) changes the solution from the base scheme $\boldsymbol{B}^*$ to the closest divergence-free discrete representation of the field, by introducing the smallest possible correction. Furthermore, the method provides a consistent

discretization without reducing the order of accuracy of the base scheme, even in presence of discontinuities.

Of course, the price one has to pay is the solution of a Poisson equation which can be rather expensive, especially on parallel computers or on adaptive grids. Under many circumstances, however, it may not be necessary to solve Eq. (91) to machine accuracy, and divergence errors may as well be kept below some predefined tolerance, typically a small fraction of the $|\nabla \cdot \boldsymbol{B}^*|$ generated in a single time step from the base scheme. This makes iterative solvers, like the conjugate gradient type linear solvers [24, 49], particularly efficient and flexible candidates to solve Eq. (91).

4.2 Constrained Transport

In the constrained transport method (CT henceforth), originally devised by [17], the induction equation is discretized by adopting a staggered representation of magnetic and electric vector fields. This formulation is better understood by integrating Faraday's law on a given surface S bounded by the curve ∂S and using Stoke's theorem to obtain a surface integration:

$$\frac{d}{dt}\int_S \boldsymbol{B}\cdot d\boldsymbol{S} = -\int_{\partial S} \Omega \cdot d\boldsymbol{l}\,, \tag{92}$$

where Ω is the electromotive force. In this form, the three components of magnetic field are evolved on the zone face to which they are orthogonal and are treated as surface averages, see Fig. 7. Each component has, therefore, a different spatial collocation in the control volume. For a Cartesian cell with lower and upper coordinate limits given by (x_-, y_-, z_-) and (x_+, y_+, z_+), the surface averaged magnetic fields are

$$\bar{B}_x^{\pm} = \frac{1}{\Delta y \Delta z}\int\int B_x(x_\pm, y, z)\, dydz\,, \tag{93}$$

$$\bar{B}_y^{\pm} = \frac{1}{\Delta x \Delta z}\int\int B_y(x, y_\pm, z)\, dxdz\,, \tag{94}$$

$$\bar{B}_z^{\pm} = \frac{1}{\Delta x \Delta y}\int\int B_z(x, y, z_\pm)\, dxdy\,, \tag{95}$$

where the integrals extend from the lower to the upper bounds of the cell and $\Delta x = x_+ - x_-$, $\Delta y = y_+ - y_-$, $\Delta z = z_+ - z_-$ are the zone widths. Note that the staggered collocation is perfectly consistent with the traditional 7-wave approach where the normal component of the field B_x is not allowed to have a jump, while the tangential components certainly can. From this perspective, B_x is regarded as a parameter when solving Riemann problems at zone interfaces and does not need to be reconstructed from the cell center, being already defined in the correct position. The discrete version of Eq. (92) reduces to

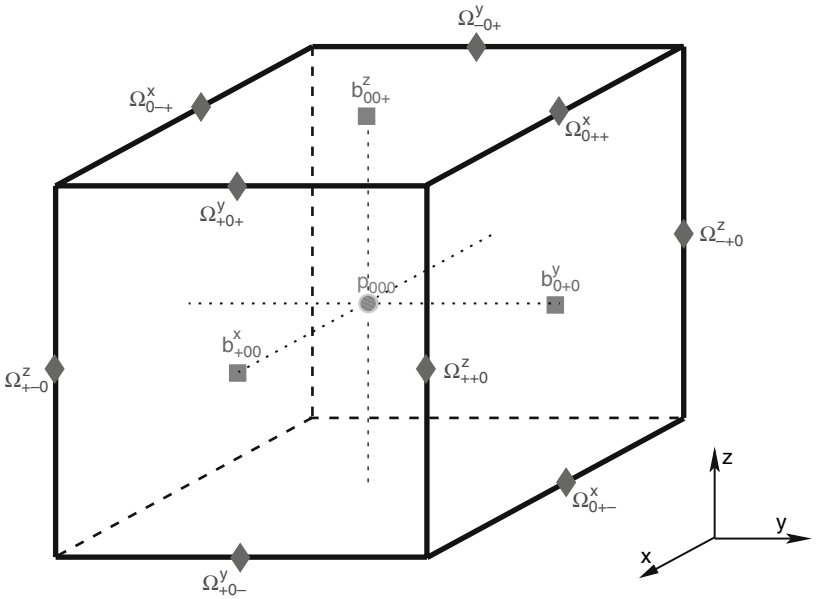

Fig. 7. Spatial collocation of flow variables in a 3D Cartesian cell. Cell-centered quantities (*circle*) include density, pressure, and velocity. Magnetic fields (*squares*) are face-centered, while electric fields (*diamonds*) are edge-centered

$$\frac{d\bar{B}_n^{\pm}}{dt} = -\sum_{m,l} \epsilon_{nml} \frac{\Delta_m \tilde{\Omega}_l^{\pm}}{\Delta h_m}\,, \tag{96}$$

where $\{n, m, l\} = x, y, z$ ($\Delta h_n = \Delta x, \Delta y, \Delta z$) and $\Delta_m \tilde{\Omega}_l$ is the difference between the line-averaged electric field

$$\tilde{\Omega}_l = \frac{1}{\Delta h_l} \int \Omega_l dh_l\,, \tag{97}$$

evaluated at opposite edges in the l-direction. In this formalism, one can verify that the divergence-free condition in its integral form,

$$\sum_n \frac{\bar{B}_n^+ - \bar{B}_n^-}{\Delta h_n} = 0\,, \tag{98}$$

is preserved to machine accuracy if the initial field has zero divergence in this discretization.

Note that the electric fields, Eq. (97), are evaluated as line integrals along the cell edges. This issue has been coped with in a number of different ways, starting with the earlier work of [3, 10, 11, 43], who incorporated the CT discretization in Godunov-type numerical schemes. Typical upwind schemes, in fact, achieve second-order accuracy by interpolating cell-centered values to

the face midpoint and then solving a Riemann problem between the resulting left and right states. Electric fields are thus available either at the cell center by properly averaging velocity and magnetic vector fields [10, 11] or at the face center using upwinded fluxes [3] from the induction equation. Therefore, some kind of spatial interpolation is required to produce the edge-centered electromotive force. In the original approach of [3], for instance, a simple arithmetic averaging between the upwind fluxes coming the four faces adjacent to a cell edge is adopted, see Fig. 8. In 2-D, for simplicity, the edge-centered electric field $\Omega \equiv \Omega_z$ is produced as:

$$\tilde{\Omega}_{i+\frac{1}{2},j+\frac{1}{2}} = \frac{\hat{\Omega}_{i+\frac{1}{2},j} + \hat{\Omega}_{i+\frac{1}{2},j+1} + \hat{\Omega}_{i,j+\frac{1}{2}} + \hat{\Omega}_{i+1,j+\frac{1}{2}}}{4} \,. \tag{99}$$

where the $\hat{\Omega}$'s follow the solution of Riemann problems at the corresponding interfaces. Despite its simplicity and effectiveness, the proposed average does

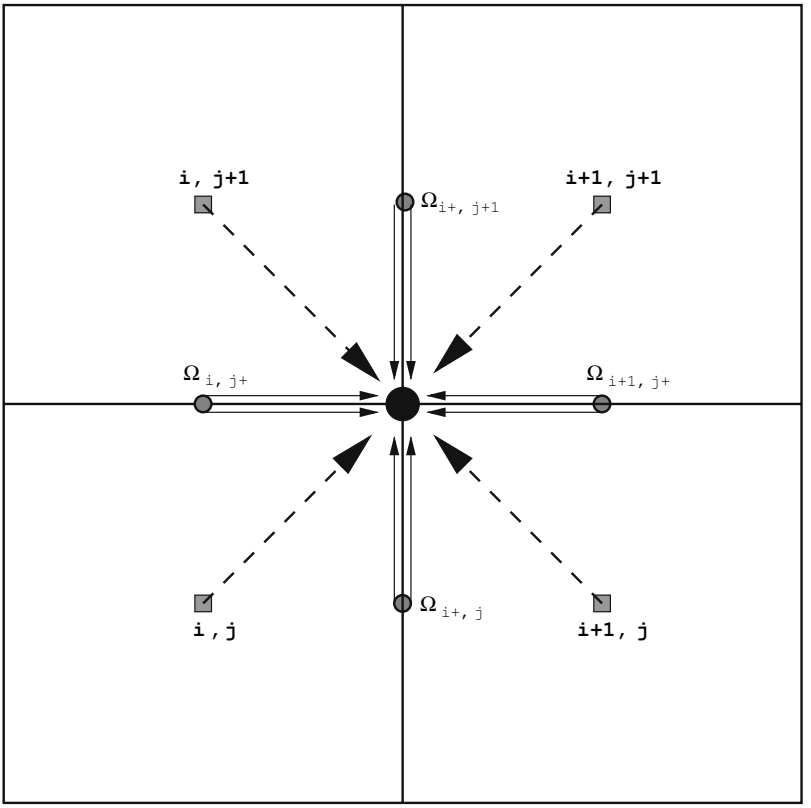

Fig. 8. Computation of the edge-centered electromotive force in 2D. The interpolation process can proceed by either averaging the vector fields available at the center (*squares* and *dashed arrows*) or the upwind fluxes available at zone interfaces (*circles* and *solid arrows*). In the picture $i+ = i + \frac{1}{2}$, $j+ = j + \frac{1}{2}$

not reduce to the equivalent solver for plane-parallel grid aligned flow. This failure can be traced back to the lack of a directional bias in the averaging formula [19]. This issue has been addressed by a number of investigators, at the same time offering alternative strategies to overcome this inconsistency.

In [29] and, more recently [30], this problem has been faced by noticing that the flux components appearing in the induction equation are defined in terms of point values at the intersections of cell faces, where different characteristic wave fans may overlap. An appropriate average of these flux components should follow a proper upwind selection rule, since a same flux component at the same collocation point results to have two independent representations in terms of characteristic wave fans. The resulting four-states combination cannot be reduced simply to an interpolation or averaging form based on the four cell-centered values of the arguments. Instead, specializing to the $\Omega \equiv \Omega_z$ flux, a single-valued numerical flux comes out by averaging over the two overlapping x and y Riemann wave fans at the $(x_{i+\frac{1}{2}}, y_{j+\frac{1}{2}})$ edge. This entails to a four-state flux function preserving the continuity and upwind properties along each direction:

$$\tilde{\Omega} = \langle \Omega \rangle - \phi_y + \phi_x \,, \tag{100}$$

where the first term $\langle \Omega \rangle$ expresses the smooth contribution, whereas ϕ_x and ϕ_y are the dissipative terms. For the HLL central-upwind scheme, for instance, smooth and dissipative terms take the form

$$\langle \Omega \rangle = \frac{\alpha_x^+ \alpha_y^+ \Omega^{\mathrm{LL}} + \alpha_x^+ \alpha_y^- \Omega^{\mathrm{LR}} + \alpha_x^- \alpha_y^+ \Omega^{\mathrm{RL}} + \alpha_x^- \alpha_y^- \Omega^{\mathrm{RR}}}{(\alpha_x^+ + \alpha_x^-)(\alpha_y^+ + \alpha_y^-)} \,, \tag{101}$$

and

$$\phi_x = \frac{\alpha_x^+ \alpha_x^-}{\alpha_x^+ + \alpha_x^-} \left(B^{\mathrm{R}}_{y,i+1,j+\frac{1}{2}} - B^{\mathrm{L}}_{y,i,j+\frac{1}{2}} \right) , \tag{102}$$

$$\phi_y = \frac{\alpha_y^+ \alpha_y^-}{\alpha_y^+ + \alpha_y^-} \left(B^{\mathrm{R}}_{x,i+\frac{1}{2},j+1} - B^{\mathrm{L}}_{x,i+\frac{1}{2},j} \right) , \tag{103}$$

where left (L) and right (R) superscripts give the corresponding interpolated point values with respect to the edge $(i+\frac{1}{2}, j+\frac{1}{2})$, see Fig. 9. In Eqs. (101), (102) and (103), $\alpha_x^\pm$ and $\alpha_y^\pm$ determine the opening of the x and y Riemann fans, in terms of estimates to the maximum (+) and minimum (−) characteristic velocities, respectively. Adopting the notations introduced in Eq. (29), one may take, for example

$$\alpha_x^\pm = \max\left(\pm\lambda^x_{S,i+\frac{1}{2},j}, \pm\lambda^x_{S,i+\frac{1}{2},j+1}, 0 \right) \tag{104}$$

where $S = R$ ($S = L$) for α_x^+ (α_x^-). Similar considerations hold for $\alpha_y^\pm$. The constructed numerical flux is consistent with the fact that each component of the induction equation, for a given velocity field and expressed in terms of the vector potential $\boldsymbol{A}$, has the form of a scalar Hamilton–Jacobi equation. This

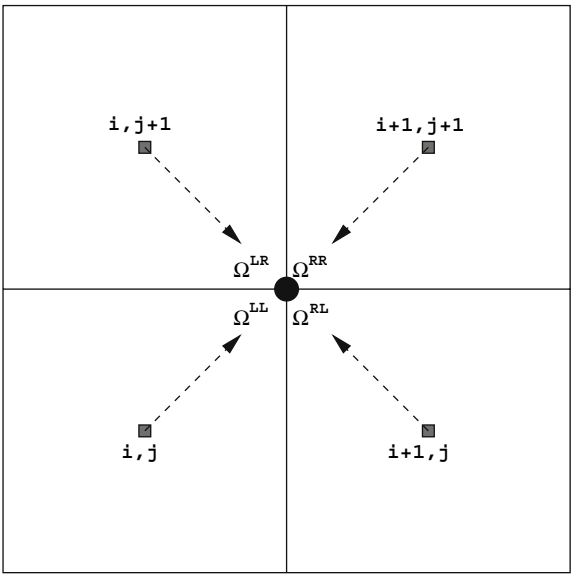

Fig. 9. Computation of the edge-centered electromotive force using the Upwind Constrained Transport (UCT) method of [30]. The four electric fields $\Omega^{\mathrm{LL}}, \Omega^{\mathrm{LR}}, \Omega^{\mathrm{RL}}$, and Ω^{RR} are reconstructed from the cell centers using two-dimensional interpolation. The edge-centered electromotive force comes by averaging the two overlapping Riemann fan at $i + \frac{1}{2}, j + \frac{1}{2}$

formalism has been successfully extended to special and general relativistic flows in [13, 14].

A different, somewhat more empirical strategy is proposed by [19], where the authors construct a more elaborate spatial integration procedure for the electric field. The reconstruction rest upon an upwind selection rule depending on the sign of the contact mode, in a way specifically designed to properly control the amount of numerical dissipation.

In [51], the induction equation is modified by introducing an additional term containing a mixed (space–time mixed) second derivative of the electric field. The sign of this extra term is chosen to control the anti dissipative effect arising from the equivalent modified equation.

References

1. Balsara, D.S., ApJS, **116**, 133 (1998) 82
2. Balsara, D.S., & Spicer, D.S., JCP, **149**, 270 (1999) 71, 77
3. Batten, P., Clarke, N., Lambert, C., & Causon, D.M., SIAM JSCom, **18**, 1553 (1997) 72, 96, 97
4. BrackBill, J.U., & Barnes, D.C., JCP, **35**, 426 (1980) 72, 91, 93, 94
5. Brio, M., & Wu, C.C., JCP, **75**, 400 (1988) 71, 75, 89

6. Cargo, P., & Gallice, G., JCP, **136**, 446 (1997) 89
7. Dai, W., & Woodward, P.R., JCP, **111**, 354 (1994) 75, 76, 79
8. Dai, W., & Woodward, P.R., JCP, **115**, 485 (1994) 75, 79
9. Dai, W., & Woodward, P.R., SIAM JSCom, **18**, 957 (1997) 75, 79
10. Dai, W., & Woodward, P.R., ApJ, **494**, 317 (1998) 71, 96, 97
11. Dai W., & Woodward, P.R., JCP, **142**, 331 (1998) 96, 97
12. Davis, S.F., SIAM JSSCom, **9**, 445 (1988) 72, 93
13. Dedner, A., Kemm, F., Kröner, D., Munz, C.-D., Schnitzer, T., & Wesenberg M., JCP, **175**, 645 (2002) 99
14. Del Zanna, L., Bucciantini, N., & Londrillo, P., A & A, **400**, 397 (2003) 99
15. Del Zanna, L., Zanotti, O., Bucciantini, N., & Londrillo, P., A & A, **473**, 11 (2007) 81
16. Einfeldt, B., SIAM JNM, **25**, 294 (1988) 81
17. Evans, C. R., & Hawley J.F., JCP, **332**, 659 (1988) 72, 95
18. Falle, S.A.E.G., Komissarov, S.S., & Joarder, P., MNRAS, **297**, 265 (1998) 75, 77, 79
19. Gardiner, T.A., & Stone, J.M., JCP, **205**, 509 (2005) 72, 98, 99
20. Godunov, S.K., DoKAN, SSSR, **139**, 521 (1972) 93
21. Gurski, K.F., SIAM JSCom, **25**, 2165 (2004) 83, 84
22. Harten A., JCP, **49**, 357 (1983) 80
23. Harten, A., Lax, P.D., & van Leer, B., SIAMR, **25**, 35 (1983) 93
24. Hestenes, M.R., & Stiefel, E., JRNBS, **49**, 409 (1954) 95
25. Jeffrey A., & Taniuti T., Non-linear wave propagation. Academic Press, New York, (1964) 76, 77
26. Kennel, C.F., Blandford, R.D., & Coppi, P., JPlPh, **42**, 299 (1989) 77
27. Lax, P.D., CPAM, **VII**, 159 (1954) 80
28. Lee, D., An Unsplit Staggered Mesh Scheme For Multidimensional Magnetohydrodynamics: A Staggered Dissipation-control Differencing Algorithm Ph.D. Thesis, University of Maryland (College Park, Md.) (2006) 83, 84
29. Li, S., JCP, **203**, 344 (2005) 72, 98
30. Londrillo, P., & Del Zanna, L., ApJ, **530**, 508 (2000) 98, 99
31. Londrillo, P., & Del Zanna, L., JCP, **195**, 17 (2004) 83
32. Mignone, A., & Bodo, G., MNRAS, **364**, 126 (2005) 83, 84
33. Mignone, A., & Bodo, G., MNRAS, **368**, 1040 (2006) 83, 88
34. Mignone, A., JCP, **225**, 1427 (2007) 75
35. Mignone, A., Bodo, G., Massaglia, S., Matsakos, T., Tesileanu, O., Zanni, C., & Ferrari, A., ApJS, **170**, 228 (2007) 85
36. Miyoshi, T., & Kusano, K., JCP, **208**, 315 (2005) 72, 92
37. Powell, K.G., ICASE report 94-24, 1994 89, 92
38. Powell, K.G., Roe, P.L., Linde, T.J., Gombosi, T.I., & De Zeeuw D.L., JCP, **154**, 284 (1999) 91
39. Quirk, J.J., IJNMJ, **18**, 555 (1994) 88
40. Roe, P.L., JCP, **43**, 357 (1981) 71, 91
41. Roe, P.L., & Balsara, D.S., SIAM JAM, **56**, 57 (1996) 80
42. Rusanov, V.V., J. Comput. Math. Phys. USSR, **1**, 267 (1961) 71, 75, 79, 89
43. Ryu, D., & Jones, T.W., ApJ, **442**, 228 (1995) 96
44. Ryu, D., Miniati D., Jones, T.W., & Frank, A., ApJ, **509**, 244 (1998) 89
45. Tanaka, T., JCP, **111**, 381 (1994) 81, 82
46. Toro, E. F., Spruce, M., & Speares, W., ShWav, **4**, 25 (1994) 81, 83, 88

47. Toro, E.F., Riemann solvers and numerical methods for fluid dynamics. Springer-Verlag, Berlin, (1997) 77, 78
48. Torrilhon, M., JPlPh, **69**, 253 (2003) 93, 94
49. Tóth, G., JCP, **161**, 605 (2000) 95
50. van der Vorst, H.A., SIAM JSSCom, **13**, 631 (1992) 71, 75
51. Zachary, A.L., Malagoli, A., & Colella, P., SIAM JSCom, **15**, 263 (1994) 99